Celest Mech Dyn Astr (2014) 119:169–206
DOI 10.1007/s10569-014-9552-9

ORIGINAL ARTICLE

Small body surface gravity fields via spherical harmonic expansions

Yu Takahashi · D. J. Scheeres

Received: 7 July 2013: / Revised: 3 February 2014 / Accepted: 6 May 2014 /
Published online: 7 June 2014
© Springer Science+Business Media Dordrecht 2014

Abstract Conventional gravity field expressions are derived from Laplace's equation, the result being the spherical harmonic gravity field. This gravity field is said to be the exterior spherical harmonic gravity field, as its convergence region is outside the Brillouin (i.e., circumscribing) sphere of the body. In contrast, there exists its counterpart called the interior spherical harmonic gravity field for which the convergence region lies within the interior Brillouin sphere that is not the same as the exterior Brillouin sphere. Thus, the exterior spherical harmonic gravity field cannot model the gravitation within the exterior Brillouin sphere except in some special cases, and the interior spherical harmonic gravity field cannot model the gravitation outside the interior Brillouin sphere. In this paper, we will discuss two types of other spherical harmonic gravity fields that bridge the null space of the exterior/interior gravity field expressions by solving Poisson's equation. These two gravity fields are obtained by assuming the form of Helmholtz's equation to Poisson's equation. This method renders the gravitational potentials as functions of spherical Bessel functions and spherical harmonic coefficients. We refer to these gravity fields as the interior/exterior spherical Bessel gravity fields and study their characteristics. The interior spherical Bessel gravity field is investigated in detail for proximity operation purposes around small primitive bodies. Particularly, we apply the theory to asteroids Bennu (formerly 1999 RQ36) and Castalia to quantify its performance around both nearly spheroidal and contact-binary asteroids, respectively.

Electronic supplementary material The online version of this article (doi:10.1007/s10569-014-9552-9) contains supplementary material, which is available to authorized users.

Y. Takahashi (✉) · D. J. Scheeres
University of Colorado at Boulder, 429 UCB, Boulder, CO 80309-0429, USA
e-mail: yu.takahashi@colorado.edu

D. J. Scheeres
e-mail: scheeres@colorado.edu

Present Address
Y. Takahashi
Jet Propulsion Laboratory/California Institute of Technology, 4800 Oak Grove Drive,
Pasadena, CA 91109, USA
e-mail: yu.takahashi@jpl.nasa.gov

Furthermore, comparisons between the exterior gravity field, interior gravity field, interior spherical Bessel gravity field, and polyhedral gravity field are made and recommendations are given in order to aid planning of proximity operations for future small body missions.

Keywords Asteroid · Gravity field · Spherical harmonics · Spherical Bessel function · Proximity operation · Laplace's equation · Poisson's equation · Brillouin sphere · Bennu · Castalia

1 Introduction

Interest in studying small bodies has been growing significantly in recent years, due to a wide spectrum of motivation arising from the study of the evolution of the Solar System, in-situ utilization of precious materials buried in small bodies, bridging the strategical knowledge gap prior to future manned mission to Mars, and understanding the potentially hazardous objects that may impact the Earth, to name a few. With advanced ground-based and space-based asteroid survey systems, we are discovering more and more asteroids, and the current number of cumulative near-Earth asteroids (NEA) reach over 10000, roughly 850 of which are larger than 1 km. The NEA search/characterization programs such as Wide-field Infrared Survey Explorer (NEO/NEOWISE), Panoramic Survey Telescope and Rapid Response System (Pan-Starrs), Catalina Sky Survey (CSS), Lincoln Near-Earth Asteroid Research (LINEAR), and Goldstone and Arecibo radars all contribute to discovering new asteroids. However, these ground/space-based observations do not fully characterize the physical properties of small bodies such as the shape, total mass, rotation state, and internal composition. These parameters can only be investigated to desired accuracy by sending a spacecraft, and accurate gravity field modeling is necessary to ensure a successful mission. It is the purpose of this paper to quantity the performance of the current gravity field modeling capabilities in the close proximity to the asteroid's surface, with main focus on the construction of a landing/touch-and-go (TAG) trajectory.

The most widely used gravitational potential expression is the exterior gravity field in Eq. (1) (Kaula 1966; Lundberg and Schutz 1988):

$$U^e = \frac{GM^*}{R_e^*} \sum_{n=0}^{\infty} \sum_{m=0}^{n} \left(\frac{R_e^*}{r}\right)^{n+1} P_{nm}(\sin\phi) \begin{bmatrix} \cos(m\lambda) \\ \sin(m\lambda) \end{bmatrix} \cdot \begin{bmatrix} C_{nm}^e \\ S_{nm}^e \end{bmatrix} \tag{1}$$

where U is the potential, e super/subscript denote the exterior quantity, G is the gravitational constant, M^* is the reference mass (nominally the total mass of the body), R^* is the reference radius (nominally the radius of the Brillouin sphere, explained below), r is the spacecraft position, P_{nm} is the associated Legendre function of degree n and order m, C_{nm} and S_{nm} are spherical harmonic coefficients, λ is longitude, and ϕ is latitude in the body-fixed frame. This exterior gravity field, as described in detail by Werner (2010), is generally valid only outside the circumscribing sphere of an asteroid, hence the name "exterior gravity field". The circumscribing sphere is also called the Brillouin sphere, within which all mass elements of the asteroid reside (Brillouin 1933). Thus, as has been shown for general body shapes, the exterior gravity field does not model the dynamical environment within the Brillouin sphere, which poses a problem when performing proximity operations around asteroids. It should be noted that the gravitation of a body with analytical structure could still be represented by the Laplace series in the shallow depth of the surface. However, the small parameter $1 - r/R$ is

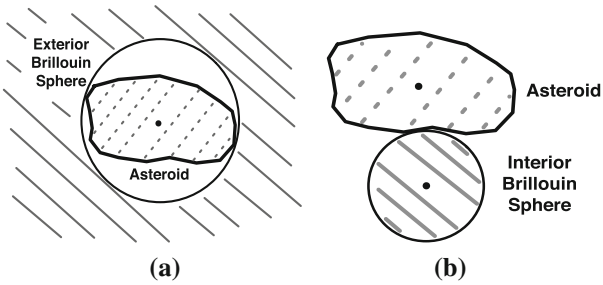

Fig. 1 Convergence regions of the exterior and interior gravity fields. **a** Exterior Brillouin sphere, **b** Interior Brillouin sphere

not negligible for asteroids with irregular topology, and the resulting gravity field does not yield accurate gravitational potential (Kholchevnikov 1971, 1972; Kholshevnikov 1977).

The exterior gravity field expression is one of spherical harmonic expansions of the gravity field, which is obtained by solving Laplace's equation by separation of variables (MacRobert 1948). In fact, the separation of variables yield two solutions for Laplace's equation, the other type of which is referred to as the interior gravity field.

$$U^i = \frac{GM^*}{R_i^*} \sum_{n=0}^{\infty} \sum_{m=0}^{n} \left(\frac{r}{R_i^*} \right)^n P_{nm}(\sin\phi) \begin{bmatrix} \cos(m\lambda) \\ \sin(m\lambda) \end{bmatrix} \cdot \begin{bmatrix} C_{nm}^i \\ S_{nm}^i \end{bmatrix} \tag{2}$$

where the i super/subscript denotes the interior quantity. The detailed derivation of interior gravity field has been published by Werner (2010), and the application of the theory is discussed by Takahashi and Scheeres (2012) and Takahashi et al. (2013). As the name implies, this interior gravity field converges interior to the Brillouin sphere and outside of the body. Both the exterior and interior gravity fields are spherical harmonic expansions of the potential, and their characteristics are well documented in the references above. The convergence region of the interior gravity field is up to a point on the surface where the interior Brillouin sphere makes a contact, which can be designated as the touchdown site for a landing trajectory. The interior Brillouin sphere is different from the exterior Brillouin sphere, and neither of them completely maps out the potential/acceleration of the gravity field around the body. Figure 1 shows the convergence regions of the exterior and interior gravity fields.

In Fig. 1, the solid lines correspond to the region of convergence, and the dotted lines correspond to the region of mass elements that contribute to the gravity field. As indicated above, the convergence regions of both the exterior and interior gravity fields exclude any mass distribution within their Brillouin spheres. The size of the interior Brillouin sphere is arbitrary so long as it is tangent to the body at one contact point (i.e., TAG point), and the performance of the interior gravity field depends on the placement of the center of the interior Brillouin sphere. The exterior gravity field does not enjoy the same liberty, and its Brillouin sphere is identical to the circumscribing sphere. One major drawback of the interior gravity field, as manifested in Fig. 1b, is that many interior gravity fields are necessary to map out the entire space of the gravity field around the body (i.e., total mapping). This problem becomes more critical when we desire to map out the gravity field in a severely concave region, which is a prominent feature of contact binaries. In contrast, the interior gravity field is shown to be accurate for regional mapping where the surface is smooth (Takahashi et al. 2013).

There are alternatives to the exterior/interior gravity fields, two most widely acquainted models of which are the polyhedral gravity field (Werner and Scheeres 1997) and mass concentration (mascon) model. However, they also have drawbacks inherent in their expressions. The polyhedral gravity field converges anywhere around the body (even on the surface) and

contains information of infinitely higher-degree and higher-order expansion of the spherical harmonic gravity fields, which are very attractive features for a gravity field expression. On the contrary, the polyhedral gravity field is computationally intensive, even though mitigation measures exist (Cangahuala 2005). Furthermore, the polyhedral gravity field assumes a known density distribution, the estimation of which is convoluted and is not unique. Takahashi and Scheeres (2013) discuss the block density estimation method to retrieve an accurate density distribution of a body by fitting it to the exterior spherical harmonic coefficients determined from the orbit determination (OD) process. However, the reconstruction of the gravity field takes prohibitively long time for timely navigation and is only applicable for post processing analysis unless interpolation techniques, such as cubed-sphere (Jones et al. 2009), MRQSphere (Jones 2010), and Fetch models (Russell and Arora 2011), are incorporated efficiently. The mascon model is inaccurate near the body surface and estimation of each mass element renders a singularity as the number of particles is increased (Park et al. 2010). A useful application of the mascon model is to estimate the mass of a particular surface feature as discussed by Gottlieb (1970), but the total mapping cannot be achieved accurately for small body navigation purposes.

In this paper, we will discuss other types of spherical harmonic expansion of the gravity field in an attempt to overcome problems discussed above. Specifically, we will solve Poisson's equation within the Brillouin sphere of the asteroid after redistribution of mass within it. This approach yields two types of solutions to the gravity field via spherical Bessel function, and we refer to them as the interior/exterior spherical Bessel gravity fields. We will mainly discuss the interior spherical Bessel gravity field as it complements the null space of the exterior gravity field.

The original work of the interior spherical Bessel gravity field is discussed by Allen et al. (1992) and Palmer (1994), and its application to asteroid gravity fields by Herrera-Sucarrat et al. (2013). Allen et al. and Palmer first discussed the derivation of the interior spherical Bessel gravity field with the dynamic propagation of celestial bodies in mind. Then, Herrera-Sucarrat et al. applied the theory to study the solutions to the equilibrium points and zero-velocity curves near the surface of small bodies, which gives qualitative insight into the performance of the interior spherical Bessel gravity field. In this paper, we will also derive the interior spherical Bessel gravity field with slightly different motivation and quantify its performance. Specifically, we will leverage the properties of the interior spherical Bessel gravity field for the proximity operation around small bodies for deep space navigation purposes. That is, the performance of the interior spherical Bessel gravity field is studied in the context of accurate trajectory design and safe navigation of a spacecraft down to the surface of a small body.

The following sections will entail the derivation of the interior spherical Bessel gravity field and its performance around asteroids (101955) Bennu (hereafter Bennu) and Castalia. Bennu is formerly known as 1999 RQ36, and it is the target body of the OSIRIS-REx mission. As the goal of the OSIRIS-REx mission is to collect samples from the asteroid's surface, thorough analysis of proximity operation is crucial. We will use the shape model determined by Nolan et al. (2013) to evaluate the gravity field environment around Bennu. While Bennu is nearly spherical in shape, Castalia is a contact binary that shows a distinct two-lobe configuration (Ostro et al. 1990; Hudson and Ostro 1994). Werner and Scheeres (1997) previously analyzed the gravity field environment near the surface of Castalia by assuming a homogeneous density and using the polyhedral gravity field. However, each lobe of Castalia could possess different density distributions, and the gravity field characterization of such an elongated body is extremely challenging. It is of our interest to evaluate the performance of the interior spherical Bessel gravity field around such an irregularly shaped body. For

both asteroids, we compare the performance of the exterior gravity field, interior gravity field, interior spherical Bessel gravity field, and polyhedral gravity field. Their accuracies are compared in context of total mapping vs. regional mapping. Finally, recommendations are given for mapping out the gravity field environment in close proximity to small body's surface for future mission planning.

2 Laplace's and Poisson's equations

In this section, we present Laplace's and Poisson's equations. Their derivations are given by, for example, MacRobert (1948) (Chapter 2 and 8). The potential of a field point placed outside the body under the influence of a body's gravity field is defined as

$$U = G \int_V \frac{\rho(\mathbf{r}')dv}{|\mathbf{r} - \mathbf{r}'|} = G \int_M \frac{1}{\Delta} dm' \tag{3}$$

where $\mathbf{r}$ is position vector, V is the total volume, v is its differential element, ρ is density as a function of the position vector of a mass element (m), M is the total mass, $\mathbf{\Delta}$ is the relative position between the field point and the mass element, and Θ is the angle between $\mathbf{r}$ and $\mathbf{r}'$ (Fig. 2). Note that the bold quantities are vectors. For all quantities associated with the mass element, we denote them with a prime. The quantities associated with the field point is left unprimed.

Then, Laplace's equation is given by computing the trace of the second-order partial of the potential as

$$\nabla^2 U = \frac{\partial^2 U}{\partial x^2} + \frac{\partial^2 U}{\partial y^2} + \frac{\partial^2 U}{\partial z^2} = tr\left(\frac{\partial^2 U}{\partial \mathbf{r}^2}\right) = 0 \tag{4}$$

which is valid anywhere outside the body. Equation (4) is satisfied by both the exterior and interior gravity fields in Eqs. (1) and (2). On the other hand, Poisson's equation states

$$\nabla^2 U = -4\pi G\rho \tag{5}$$

which is valid anywhere inside the body. Now that we have two equations that are valid inside/outside the body, it seems natural to solve Poisson's/Laplace's equations directly and attempt to map out the gravity field within/around the body in its entirety. However, there is subtle difficulty that we immediately notice when we graphically show the solution space. Figure 3 shows the regions where Laplace's and Poisson's equations are satisfied along with the convergence regions of the exterior and interior gravity fields.

In Fig. 3, the white body is the asteroid, within which Poisson's equation must be satisfied. The dark gray regions are the convergence regions of the exterior and interior gravity fields

Fig. 2 Potential definition

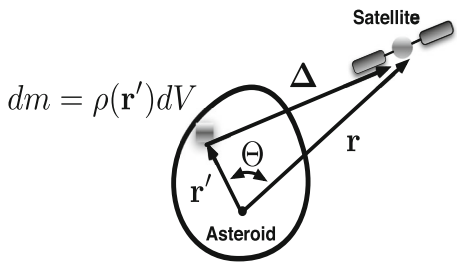

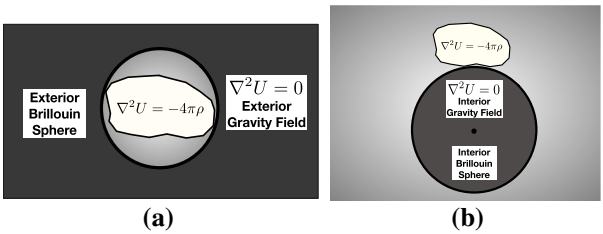

(a) **(b)**

Fig. 3 Solution space of Laplace's and Poisson's equations. **a** Exterior gravity field, **b** Interior gravity field

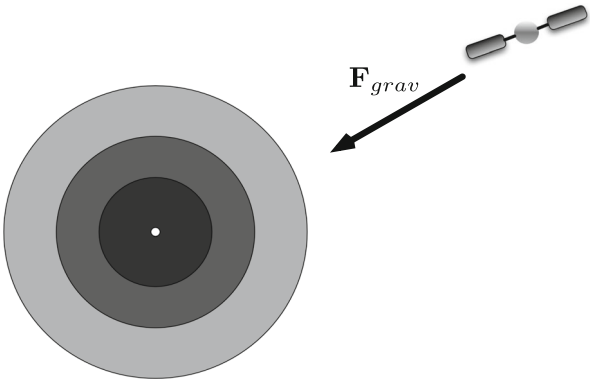

Fig. 4 Gravity field by concentric spheres and shells of the same mass

which satisfy Laplace's equation, and the faded gray regions exist without a corresponding gravity field expression. Thus, even if the solutions are obtained for both Laplace's and Poisson's equations, the null space of the gravity field is still present, and directly solving Poisson's equation seems rather fruitless effort.

3 Redistribution of the mass within the circumscribing sphere

Based on the discussion in the previous section, it appears that we are still facing the same problem as before even after solving Poisson's equation. That is, the proximity region to the surface does not have a well-defined gravity field expression. Before we further proceed, we make a few notes about the relation between the gravity field and the mass distribution. From Eq. (3), the gravitational potential is clearly a function of the mass distribution, and forward modeling of the potential, given a particular set of mass distribution, is straightforward. For example, the polyhedral gravity field by Werner and Scheeres (1997) is particularly useful for this purpose. However, estimation of the mass distribution for a given gravity field is not trivial, as discussed by Takahashi and Scheeres (2013) among many others.

For example, in Fig. 4, the spacecraft feels the gravitation due to the concentric spheres and shells of the same mass. These spheres and shells exert the same force on the spacecraft, and it is impossible to distinguish one model from another by gravity field measurement unless constraints can be put on the mass distribution through the shape model and surface/internal composition. This simple example illustrates that the inversion process is not unique, and infinitely many solutions of density distribution exist for a given gravity field.

On the other hand, if we change our point of view, the same example shows that we need not have the exact mass distribution in order to model the sensed gravity field accurately. That is, the disadvantage of not being able to constrain the mass distribution can be turned into

our advantage. Therefore, it becomes viable again to solve Poisson's equation and obtain the solution, with the condition that the solution space terminates at the boundary of the exterior/interior Brillouin spheres, merging smoothly into the exterior/interior gravity fields.

4 Solution of Poisson's equation via spherical Bessel function

In this section, we solve Poisson's equation. To this end, we consider the solution to the equation of generic form given below:

$$\nabla^2\psi + k^2\psi = 0 \tag{6}$$

Equation (6) is classified as Helmholtz's equation when $k^2 > 0$, where k is a constant and not imaginary. By comparing Eqs. (5) and (6), we observe remarkable similarity between Poisson's and Helmholtz's equations. In Eq. (5), none of the variables on the right-hand side are negative. Thus, when the whole term is moved to the left-hand side of the equation, we have $k^2 > 0$, only missing the factor of ψ. As a matter of fact, Poisson's equation can be solved by assuming the form of Helmholtz's equation, and we perform such an analysis in the following.

4.1 Poisson's equation as Helmholtz's equation

Poisson's equation is solved by combining the work by Allen et al. (1992), Palmer (1994), and separation of variables (MacRobert 1948; Pinsky 1984; Hanna and Rowland 1990). Poisson's equation (Eq. 5), assuming the form of the Helmholtz's equation, states that

$$\nabla^2 V = -4\pi G\rho = -k^2 V \tag{7}$$

where V is used for potential and shall not be confused with the volume of the asteroid. For the rest of the paper, the potential U is used for the solutions to Laplace's equation, and V is used for the solutions to Poisson's equation. Equation (7) is equivalent to expressing the density as a function of the potential.

$$\rho = \frac{k^2 V}{4\pi G} \tag{8}$$

It is worthwhile to pause for a moment and ponder the meaning of Eq. (8). The equation states that the density distribution conforms to the potential distribution, scaled by the coefficient k ($k = 0$ yields Laplace's equation). That is, Eq. (8) translates to artificially redistributing the mass in the solution space to obtain the desired gravity field. As shown in Fig. 3, the null space of the gravity field is inside the exterior Brillouin sphere and outside the interior Brillouin sphere. Therefore, we redistribute the mass of the asteroid inside the exterior Brillouin sphere and outside the interior Brillouin sphere to obtain two types of solutions to Poisson's equation. As these boundaries form a sphere, it is natural to solve Eq. (7) in the spherical coordinates (r, λ, ϕ).

4.2 Radial potential expression

We apply separation of variables to the potential expression in spherical coordinates. We set $V = R(r)\Phi(\phi)\Lambda(\lambda)$ and use Eq. (7) to get

$$\left[\frac{1}{R(r)}\left(r^2\frac{\partial^2 R(r)}{\partial r^2}+2r\frac{\partial R(r)}{\partial r}\right)+k^2r^2\right]$$
$$+\left[\frac{1}{\Phi(\phi)}\left(\frac{\partial^2\Phi(\phi)}{\partial\phi^2}-\tan\phi\frac{\partial\Phi(\phi)}{\partial\phi}\right)\right]+\left[\frac{1}{\cos^2\phi\Lambda(\lambda)}\frac{\partial^2\Lambda(\lambda)}{\partial\lambda^2}\right]=0 \tag{9}$$

where $R(r)$ is the radial potential, $\Phi(\phi)$ is the latitudinal potential, and $\Lambda(\lambda)$ is the longitudinal potential. Notice that the expressions in the second and the third brackets are independent of r, and therefore, so is the first. As the sum of three terms yields zero, the first term and the sum of the second and the third terms must be a constant with opposite signs. We set the constant value of the first term to $n(n+1)$ to get

$$\frac{\partial^2 R(r)}{\partial r^2}+\frac{2}{r}\frac{\partial R(r)}{\partial r}+\left[k^2-\frac{n(n+1)}{r^2}\right]R(r)=0 \tag{10}$$

The solution of $R(r)$ is the spherical Bessel function of the first kind $j_n(k_{ln}r)$ and second kind $\mathcal{Y}_n(k_{ln}r)$, which are defined as

$$j_n(x)=\sqrt{\frac{\pi}{2x}}J_{n+\frac{1}{2}}(x) \tag{11}$$

$$\mathcal{Y}_n(x)=\sqrt{\frac{\pi}{2x}}Y_{n+1/2}(x)=(-1)^{n+1}j_{-(n+1)}(x) \tag{12}$$

where J_n and Y_n are the Bessel functions of first and second kind, respectively. The subscript n is referred to as the order of the Bessel function by convention, but we use the term "degree" instead. The meaning of the l subscript for constant k will be clarified in Sect. 4.5. The Bessel function and spherical Bessel function of second kind are also known as Weber's function and spherical Neumann function, respectively. For the rest of the paper, $j_n(x)$ is referred to as the spherical Bessel function and $\mathcal{Y}_n(x)$ the spherical Neumann function. The spherical Neumann function of degree n is conventionally denoted as $n_n(x)$, but we will adopt $\mathcal{Y}_n(x)$ to avoid confusion with the degree n. Note that $j_n(x)$ is defined everywhere for $x\geq 0$, but $\mathcal{Y}_n(x)$ tends to negative infinity as $x\to 0$. Thus, the solution by j_n is used to describe the gravity field inside the exterior Brillouin sphere, and that by $\mathcal{Y}_n$ to describe the gravity field outside the interior Brillouin sphere.

4.3 Longitudinal potential expression

Now that the radial potential $R(r)$ is obtained, $\Lambda(\lambda)$ and $\Phi(\phi)$ remain to be solved. We first find the solutions to $\Lambda(\lambda)$. After multiplying both sides of Eq. (9) by $\cos^2\phi$, we obtain

$$\frac{\cos^2\phi}{\Phi(\phi)}\frac{\partial^2\Phi(\phi)}{\partial\phi^2}-\frac{\sin\phi\cos\phi}{\Phi(\phi)}\frac{\partial\Phi(\phi)}{\partial\phi}+n(n+1)\cos^2\phi=-\frac{1}{\Lambda(\lambda)}\frac{\partial^2\Lambda(\lambda)}{\partial\lambda^2} \tag{13}$$

Now we have separated the terms to those dependent only on ϕ and λ. Thus, the terms on either side of the equation must be a constant. We set the term on the right-hand side of the equation to m^2 and get

$$\Lambda(\lambda)=\mathscr{A}_{lnm}\cos m\lambda+\mathscr{B}_{lnm}\sin m\lambda \tag{14}$$

which is a simple harmonic oscillator. The coefficients $\mathscr{A}_{lnm}$ and $\mathscr{B}_{lnm}$ define the amplitude of the function $\Lambda(\lambda)$. The subscript m is defined as the order of the gravity field.

4.4 Latitudinal potential expression

For $\Phi(\phi)$, we have

$$\frac{\partial^2 \Phi(\phi)}{\partial \phi^2} - \tan\phi \frac{\partial \Phi(\phi)}{\partial \phi} + \left[n(n+1) - \frac{m^2}{\cos^2\phi} \right] \Phi(\phi) = 0 \tag{15}$$

We substitute $\xi = \sin\phi$ to get the Legendre's associated equation. Its solution is given by, for example, MacRobert (1948) (Chapter 4) as

$$\Phi(\phi) = P_{nm}(\sin\phi) \tag{16}$$

which is the associated Legendre function of degree n and order m.

4.5 Interior and exterior spherical Bessel gravity fields

Finally, we combine the solutions for $R(r)$, $\Lambda(\lambda)$, and $\Phi(\phi)$ to obtain

$$V^i = \sum_{l=0}^{\infty} \sum_{n=0}^{\infty} \sum_{m=0}^{n} j_n(k_{ln}^i r) P_{nm}(\sin\phi) \left(\mathscr{A}_{lnm}^i \cos m\lambda + \mathscr{B}_{lnm}^i \sin m\lambda \right) \tag{17}$$

$$V^e = \sum_{l=0}^{\infty} \sum_{n=0}^{\infty} \sum_{m=0}^{n} \mathcal{Y}_n(k_{ln}^e r) P_{nm}(\sin\phi) \left(\mathscr{A}_{lnm}^e \cos m\lambda + \mathscr{B}_{lnm}^e \sin m\lambda \right) \tag{18}$$

where V^i is the interior spherical Bessel gravity field, and V^e is the exterior spherical Bessel gravity field (i.e., spherical Neumann gravity field). Accordingly, $\mathscr{A}_{lnm}^i$ and $\mathscr{B}_{lnm}^i$ are referred to as the interior spherical Bessel coefficients, and $\mathscr{A}_{lnm}^e$ and $\mathscr{B}_{lnm}^e$ as the exterior spherical Bessel coefficients. These two Bessel gravity fields complement the solution space of the exterior/interior spherical harmonic gravity fields (Fig. 5). Note that both V^i and V^e are other solution forms of the spherical harmonic potential expression as they contain the surface spherical harmonic potential $\mathscr{H}_{nm}$ [see Eq. (55)].

In Eqs. (17) and (18), both the interior and exterior spherical Bessel gravity fields are summed over l, n, and m, as each different value of k, n, and m satisfy Poisson's equation, and a linear combination of solutions is also a solution. For the rest of the paper, the l subscript is referred to as the "power" of the spherical Bessel function. Thus, we have degree n, order m, and power l for the Bessel gravity fields. Note that we do not sum over k, as k is a function

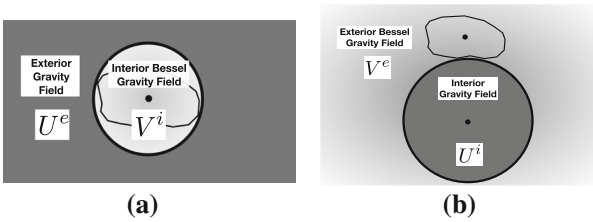

Fig. 5 Solution space of the exterior/interior spherical harmonic gravity fields and interior/exterior spherical Bessel gravity fields. The *dark gray* regions are the solution space of the exterior/interior gravity fields obtained from Laplace's equation. The *faded gray* regions are the solution space of the interior/exterior spherical Bessel gravity fields obtained from Poisson's equation. Note that the whole body of the asteroid is within the solution space of the interior/exterior spherical Bessel gravity fields. **a** Exterior gravity field and interior spherical Bessel gravity field. **b** Interior gravity field and exterior spherical Bessel gravity field

of n [see Eq. (10)] and is not a simple integer. Particular values of k_{ln}, which are different for the interior and exterior expansions, are discussed later when the boundary conditions are applied. The dependence of k on n is more apparent in Eq. (40), where the boundary condition has to be satisfied for each degree n of spherical Bessel function.

The following sections will focus on the interior spherical Bessel gravity field, as its computation directly gives the gravitation within the exterior Brillouin sphere. Detailed descriptions of the exterior spherical Bessel gravity field are given in Appendix I. Please note that, due to the large volume of material, all appendices are in the supplemental material linked to the online version of this paper. Appendices A and B are in one documentation, and appendices C through I are in another.

5 Structure of the interior spherical Bessel coefficients

In this section, we derive the explicit expressions for the interior spherical Bessel coefficients. To do so, we first rewrite Eq. (17) as

$$V^i = \frac{GM^*}{R_e^*} \sum_{l=0}^{\infty} \sum_{n=0}^{\infty} \sum_{m=0}^{n} j_n \left(\frac{\alpha_{ln}^i r}{R_e^*} \right) P_{nm}(\sin\phi) \begin{bmatrix} \cos(m\lambda) \\ \sin(m\lambda) \end{bmatrix} \cdot \begin{bmatrix} \mathscr{A}_{lnm}^i \\ \mathscr{B}_{lnm}^i \end{bmatrix} \tag{19}$$

where the coefficients $\mathscr{A}_{lnm}^i$ and $\mathscr{B}_{lnm}^i$ were scaled by a factor of R^*/M^*G (the same notation of $\mathscr{A}_{lnm}^i$ and $\mathscr{B}_{lnm}^i$ is maintained). In addition, we introduced the non-dimensionalized parameter

$$\alpha_{ln}^i = R_e^* k_{ln}^i \tag{20}$$

which is the eigenvalue of the spherical Bessel function (Watson 1944; Liu and Zou 2007). Note that the *exterior* reference radius (R_e^*) is used to non-dimensionalize the *interior* spherical Bessel coefficients ($\mathscr{A}_{lnm}^i$ and $\mathscr{B}_{lnm}^i$). This is not a misprint, and the reason will become clear in Sect. 6.

5.1 Density distribution for the interior spherical Bessel gravity field

The direct substitution of Eq. (19) into Eq. (8) renders the density distribution as

$$\rho_i = \frac{M^*}{4\pi R_e^{*3}} \sum_{l=0}^{\infty} \sum_{n=0}^{\infty} \sum_{m=0}^{n} \alpha_{ln}^{i2} j_n \left(\frac{\alpha_{ln}^i r}{R_e^*} \right) P_{nm} \begin{bmatrix} \cos(m\lambda) \\ \sin(m\lambda) \end{bmatrix} \cdot \begin{bmatrix} \mathscr{A}_{lnm}^i \\ \mathscr{B}_{lnm}^i \end{bmatrix} \tag{21}$$

It turns out that we can express $\mathscr{A}_{lnm}^i$ and $\mathscr{B}_{lnm}^i$ via the volume integral of density over the Brillouin sphere, which is discussed in the following sections.

5.2 Unnormalized interior spherical Bessel coefficients

The interior spherical Bessel coefficients are obtained by leveraging the orthogonal properties of the associated Legendre function and the spherical Bessel function. The orthogonality relationship of the associated Legendre function, using the same notation as Werner (2010), is given as

$$\iint_\sigma S_{nmi} S_{rst} \, d\sigma = \begin{cases} 0 & \text{for} \quad n \neq r \text{ or } m \neq s \text{ or } i \neq t \\ 4\pi \dfrac{(n+m)!}{(n-m)!(2n+1)(2-\delta_{0m})} & \text{for} \quad n = r \text{ and } m = s \text{ and } i = t \end{cases} \tag{22}$$

where δ is Kronecker delta function, σ is the unit sphere, and S_{nmi} is defined as

$$S_{nmi} = \begin{cases} P_{nm}(\sin\phi)\cos m\lambda \ , \ i = 0 \\ P_{nm}(\sin\phi)\sin m\lambda \ , \ i = 1 \end{cases} \tag{23}$$

Also, we have the orthogonality relationship of spherical Bessel function if both $\alpha_{\mu n}$ and $\alpha_{\nu n}$ are the roots of j_n (Arfken 1985, Chapter 11.7). However, in our case, $\alpha_{\mu n}$ and $\alpha_{\nu n}$ are both the roots of j_{n-1}. This condition arises due to the boundary conditions that we enforce on the exterior Brillouin sphere and is explained in Sect. 7. The orthogonality of j_n for such a case is derived in Appendix E.2 (Equation E.18) and given as

$$\int_0^{R^*} j_n\left(\alpha_{\mu n}\frac{r}{R^*}\right) j_n\left(\alpha_{\nu n}\frac{r}{R^*}\right) r^2 dr = \frac{R^{*3}}{2}\left[j_n(\alpha_{\mu n})\right]^2 \delta_{\mu\nu}$$
$$\text{for} \begin{cases} j_{n-1}(\alpha_{\mu n}) = 0 \\ j_{n-1}(\alpha_{\nu n}) = 0 \end{cases} \tag{24}$$

Therefore, taking the integral of the cosine term of the density, with appropriate multiplication factor, over the whole Brillouin sphere yields

$$\int_V j_n\left(\frac{\alpha^i_{ln} r'}{R^*_e}\right) P_{nm}(\sin\phi')\cos(m\lambda')\rho_i dv = \frac{\mathscr{A}^i_{lnm} M^* \mathscr{E}^i_n(\alpha^i_{ln})(n+m)!}{2(2-\delta_{0m})(2n+1)(n-m)!} \tag{25}$$

where $\mathscr{E}^i_q(\alpha^i_{ln}) = \alpha^{i2}_{ln}\left[j_q(\alpha^i_{ln})\right]^2$, $dv = r^2\sin\theta dr d\phi d\lambda$, and $\theta = \pi/2 - \phi$ (i.e., the colatitude). We can perform similar operation for the sine term of the density to get

$$\begin{cases} \mathscr{A}^i_{lnm} = \dfrac{2(2-\delta_{0m})(2n+1)(n-m)!}{M^*\mathscr{E}^i_n(\alpha^i_{ln})(n+m)!}\displaystyle\int_M j_n\left(\frac{\alpha^i_{ln} r'}{R^*_e}\right) P_{nm}(\sin\phi')\cos(m\lambda')dm' \\ \mathscr{B}^i_{lnm} \overset{m\geq 0}{=} \dfrac{4(2n+1)(n-m)!}{M^*\mathscr{E}^i_n(\alpha^i_{ln})(n+m)!}\displaystyle\int_M j_n\left(\frac{\alpha^i_{ln} r'}{R^*_e}\right) P_{nm}(\sin\phi')\sin(m\lambda')dm' \end{cases} \tag{26}$$

where $dm' = \rho_i dv$ is substituted. Notice the remarkable similarities between the interior spherical Bessel coefficients and the exterior spherical harmonic coefficients:

$$\begin{cases} C^e_{nm} = \dfrac{(2-\delta_{0,m})}{M^*}\dfrac{(n-m)!}{(n+m)!}\displaystyle\int_M \left(\frac{r'}{R^*_e}\right)^n P_{nm}(\sin\phi')\cos(m\lambda')dm' \\ S^e_{nm} \overset{m\geq 0}{=} \dfrac{2}{M^*}\dfrac{(n-m)!}{(n+m)!}\displaystyle\int_M \left(\frac{r'}{R^*_e}\right)^n P_{nm}(\sin\phi')\sin(m\lambda')dm' \end{cases} \tag{27}$$

5.3 Normalized interior spherical Bessel coefficients

For the normalized coefficients, we have

$$\begin{cases} \bar{\mathscr{A}}^i_{lnm} = \dfrac{2}{M^*\mathscr{E}^i_n(\alpha^i_{ln})}\sqrt{\dfrac{(2-\delta_{0m})(2n+1)(n-m)!}{(n+m)!}}\displaystyle\int_M j_n\left(\frac{\alpha^i_{ln} r'}{R^*_e}\right) P_{nm}(\sin\phi')\cos(m\lambda')dm' \\ \bar{\mathscr{B}}^i_{lnm} \overset{m\geq 0}{=} \dfrac{2}{M^*\mathscr{E}^i_n(\alpha^i_{ln})}\sqrt{\dfrac{2(2n+1)(n-m)!}{(n+m)!}}\displaystyle\int_M j_n\left(\frac{\alpha^i_{ln} r'}{R^*_e}\right) P_{nm}(\sin\phi')\sin(m\lambda')dm' \end{cases} \tag{28}$$

which are comparable to the normalized exterior spherical harmonic coefficients:

$$\begin{cases} \bar{C}^e_{nm} = \dfrac{1}{M^*}\sqrt{\dfrac{(2-\delta_{0m})(n-m)!}{(2n+1)(n+m)!}} \displaystyle\int_M \left(\frac{r'}{R^*_e}\right)^n P_{nm}(\sin\phi')\cos(m\lambda')dm' \\ \bar{S}^e_{nm} \overset{m>0}{=} \dfrac{1}{M^*}\sqrt{\dfrac{2(n-m)!}{(2n+1)(n+m)!}} \displaystyle\int_M \left(\frac{r'}{R^*_e}\right)^n P_{nm}(\sin\phi')\sin(m\lambda')dm' \end{cases} \tag{29}$$

where the normalization factor N_{nm} is defined as

$$N_{nm} = \sqrt{(2-\delta_{0,m})(2n+1)\frac{(n-m)!}{(n+m)!}} \tag{30}$$

This normalization factor N_{nm} is discussed in many literatures (e.g., Kaula 1966) and is introduced to alleviate the machine overflow and underflow. The normalization factor is applied to the spherical harmonics as well as the associated Legendre function so that the product of the two quantities yields the same value in the potential expressions.

6 Exterior gravity field expressed via spherical Bessel function

The relationship between the exterior gravity field (U^e) and the interior spherical Bessel gravity field (V^i) becomes clear when we express the exterior gravity field via spherical Bessel function, as was done by Allen et al. (1992), Palmer (1994), and Herrera-Sucarrat et al. (2013). As they only provide the final expression, we will clarify its origin and motivation of such mathematical reformulation.

The two potential expressions given in Eqs. (1) and (19) are derived by solving Laplace's and Poisson's equations, respectively. As we saw in Sect. 4, they complement the solution space of each other, sharing their common boundary which is the exterior Brillouin sphere. As the gravitational potential is a smooth function, these potential expressions cannot have discontinuity on the boundary of the exterior Brillouin sphere. Therefore, we impose a constraint that the potentials given by U^e and V^i match on the boundary of the exterior Brillouin sphere.

From Eq. (1), the exterior potential on the boundary of the exterior Brillouin sphere is given as

$$U^e\big|_{r=R^*_e} = \frac{GM^*}{R^*_e}\sum_{n=0}^{\infty}\sum_{m=0}^{n} P_{nm}(\sin\phi)\begin{bmatrix}\cos(m\lambda)\\ \sin(m\lambda)\end{bmatrix}\cdot\begin{bmatrix}C^e_{nm}\\ S^e_{nm}\end{bmatrix} \tag{31}$$

Similarly, from Eq. (19), the interior spherical Bessel potential on the boundary of the exterior Brillouin sphere is given as

$$V^i\Big|_{r=R^*_e} = \frac{GM^*}{R^*_e}\sum_{l=0}^{\infty}\sum_{n=0}^{\infty}\sum_{m=0}^{n} j_n\left(\alpha^i_{ln}\right) P_{nm}(\sin\phi)\begin{bmatrix}\cos(m\lambda)\\ \sin(m\lambda)\end{bmatrix}\cdot\begin{bmatrix}\mathscr{A}^i_{lnm}\\ \mathscr{B}^i_{lnm}\end{bmatrix} \tag{32}$$

As we must have the condition $U^e|_{r=R^*_e} = V^i\big|_{r=R^*_e}$, comparison of the two equations immediately yields

$$\begin{cases} C^e_{nm} = \sum_{l=0}^{\infty} j_n(\alpha^i_{ln})\mathscr{A}^i_{lnm} \\ S^e_{nm} = \sum_{l=0}^{\infty} j_n(\alpha^i_{ln})\mathscr{B}^i_{lnm} \end{cases} \tag{33}$$

Equation (33) puts a constraint on the possible values of the interior spherical Bessel coefficients. In so many words, the exterior spherical harmonic coefficients are weighted sum of the interior spherical Bessel coefficients, the weight function being the spherical Bessel function evaluated with the eigenvalue of the same degree and power. Given this result, the exterior gravity field can be expressed in terms of the interior spherical Bessel coefficients as

$$U^e = \frac{GM^*}{R^*_e} \sum_{l=0}^{\infty}\sum_{n=0}^{\infty}\sum_{m=0}^{n} j_n(\alpha^i_{ln}) \left(\frac{R^*_e}{r}\right)^{n+1} P_{nm}(\sin\phi) \begin{bmatrix} \cos(m\lambda) \\ \sin(m\lambda) \end{bmatrix} \cdot \begin{bmatrix} \mathscr{A}^i_{lnm} \\ \mathscr{B}^i_{lnm} \end{bmatrix} \tag{34}$$

The specific values of the eigenvalue α^i_{ln} necessary to compute the spherical Bessel function are discussed in the next section.

7 Boundary conditions and eigenvalues of the interior spherical Bessel gravity field

In this section, we wish to obtain the necessary conditions for the eigenvalues α^i_{ln} from the boundary conditions. On the boundary of the exterior Brillouin sphere, the acceleration of the field point must match between the exterior gravity field and the interior spherical Bessel gravity field. We already know that the azimuthal and polar components of the acceleration are matched as we have the equivalent radial component $j_n(\alpha^i_{ln})$ at $r = R^*_e$ [Eqs. (31) and (32)]. Consequently, the necessary condition for α^i_{ln} falls out by matching the radial component of the acceleration. This boundary condition is conveniently expressed by working with Eq. (34). As with the interior spherical Bessel potential, the potential expression in Eq. (34) can be obtained via separation of variables. That is, $U^e_{lnm} = R^e_{ln}(r)\Phi^e_{nm}(\phi)\Lambda^e_m(\lambda)$, where the exterior radial potential is given as

$$R^e_{ln}(r) = \frac{GM^*}{R^*_e} j_n(\alpha^i_{ln}) \left(\frac{R^*_e}{r}\right)^{n+1} \tag{35}$$

Then, the radial component of the acceleration $\ddot{r}_{lnm}$ due to the exterior gravity field, expressed via the interior spherical Bessel coefficients of degree n, order m, and power l is computed as

$$\ddot{r}_{lnm}|_{r=R^*_e} = \left.\frac{\partial R^e_{ln}(r)}{\partial r}\right|_{r=R^*_e} = -(n+1)\frac{GM^*}{R^{*2}_e} j_n(\alpha^i_{ln}) \tag{36}$$

In Eq. (36), we dropped $\Phi^e_{nm}(\phi)$ and $\Lambda^e_m(\lambda)$ (i.e., exterior latitudinal and longitudinal potentials) as neither of them is a function of r. Then, Eq. (36) constitutes the boundary condition for the interior spherical Bessel gravity field. Similarly, we compute $\ddot{r}_{lnm}$ from V^i, which requires the partial derivative of $j_n(\alpha^i_{ln} r/R^*_e)$. Arfken (1985, Section 11.7) gives useful expressions of the recurrence theorem and the derivative of $j_n(x)$:

$$j_{n+1}(x) = \frac{2n+1}{x} j_n(x) - j_{n-1}(x) \tag{37}$$

$$(2n+1)\frac{\partial\left[j_n(x)\right]}{\partial x} = nj_{n-1}(x) - (n+1)j_{n+1}(x) \tag{38}$$

Thus, we get

$$\ddot{r}_{lnm}|_{r=R_e^*} = \frac{GM^*\alpha_{ln}^i}{R_e^{*2}} j_{n-1}(\alpha_{ln}^i) - (n+1)\frac{GM^*}{R_e^{*2}} j_n\left(\alpha_{ln}^i\right) \tag{39}$$

The second component is identical to Eq. (36). Therefore, the first term needs to vanish. Accordingly, the eigenvalues are given by the condition

$$j_{n-1}(\alpha_{ln}^i) = 0 \tag{40}$$

The eigenvalues satisfying Eq. (40) can be obtained by, for example, the Newton-Raphson method and are given in Appendix F. From the properties of the spherical Bessel function, there are no repeated roots for different degree n, except at zero, and all other eigenvalues are real and positive. Careful inspection of the behavior of j_n reveals that, for the zeroth-power interior spherical Bessel coefficients, only α_{00}^i and α_{01}^i are non-zero, and all other α_{0n}^i for $n > 1$ are zero. Thus, by the definition of the interior spherical Bessel coefficients [Eqs. (26) and (28)], there are only the zeroth and first-degree interior spherical Bessel coefficients for the zeroth power (i.e., $\mathscr{A}_{000}^i$, $\mathscr{A}_{010}^i$, $\mathscr{A}_{011}^i$, and $\mathscr{B}_{011}^i$ only).

Abramowitz and Stegun (1972) list the lower-degree spherical Bessel functions, and analytical solutions are obtained up to the second degree by Allen et al. (1992). We also summarize these quantities in Appendix G.1.

8 Analytical conversion between the exterior spherical harmonic coefficients and interior spherical Bessel coefficients

In this section, we investigate the conversion method between the exterior spherical harmonic coefficients and the interior spherical Bessel coefficients. The same method is discussed by Herrera-Sucarrat et al. (2013), but we will provide more intermediate steps to indicate how the process can be generalized in future research. Recall that as we matched the potentials of both expansions on the boundary of the exterior Brillouin sphere, we obtained Eq. (33), which showed that the exterior spherical harmonic coefficients are weighted sum of the interior spherical Bessel coefficients. We further put a constraint on the possible values of the interior spherical Bessel coefficients from the density distribution.

In order for the solutions to Poisson's equation to make a smooth transition to Laplace's equation, the density distribution evaluated on the boundary of the exterior Brillouin sphere has to reach the limit

$$\lim_{r\to R_e^*} \rho_i(r,\phi,\lambda) = 0 \tag{41}$$

for all ϕ and λ except points lying on the circumscribing sphere. For small bodies, there is only one such point. Then, from Eq. (21), we have to satisfy

$$\begin{cases} \displaystyle\sum_{l=0}^{\infty} \alpha_{ln}^{i2} j_n(\alpha_{ln}^i)\mathscr{A}_{lnm}^i = 0 \\ \displaystyle\sum_{l=0}^{\infty} \alpha_{ln}^{i2} j_n(\alpha_{ln}^i)\mathscr{B}_{lnm}^i = 0 \end{cases} \tag{42}$$

Now, we wish to combine Eqs. (33) and (42) into one equation. Before we proceed, we make a remark that α^i_{0n} is non-zero only for $n = 0$ and 1, as mentioned earlier. We denote the first non-zero α^i_{ln} as $\alpha^i_{l^*n}$:

$$l^* = \begin{cases} 0, & \text{for } n = 0, 1 \\ 1, & \text{for } \ n > 1 \end{cases} \tag{43}$$

Then, we can expand Eq. (33) as

$$j_n(\alpha^i_{l^*n})\mathscr{A}^i_{l^*nm} = C^e_{nm} - \sum_{l=l^*+1}^{\infty} j_n(\alpha^i_{ln})\mathscr{A}^i_{lnm} \tag{44}$$

Also, Eq. (42) can be expanded as

$$\alpha^{i2}_{l^*n}\left[C^e_{nm} - \sum_{l=l^*+1}^{\infty} j_n(\alpha^i_{ln})\mathscr{A}^i_{lnm}\right] + \sum_{l=l^*+1}^{\infty} \alpha^{i2}_{ln} j_n(\alpha^i_{ln})\mathscr{A}^i_{lnm} = 0 \tag{45}$$

where we separated the term due to $l = l^*$ and substituted Eq. (44). By rearranging Eq. ((45), we get

$$\begin{cases} C^e_{nm} = \displaystyle\sum_{l=l^*+1}^{\infty}\left(1 - \frac{\alpha^{i2}_{ln}}{\alpha^{i2}_{l^*n}}\right) j_n(\alpha^i_{ln})\mathscr{A}^i_{lnm} \\ S^e_{nm} = \displaystyle\sum_{l=l^*+1}^{\infty}\left(1 - \frac{\alpha^{i2}_{ln}}{\alpha^{2}_{l^*n}}\right) j_n(\alpha^i_{ln})\mathscr{B}^i_{lnm} \end{cases} \tag{46}$$

Equation (46) states that the weighted sum of the interior spherical Bessel coefficients must converge to the exterior spherical harmonic coefficients. However, the exact values of the interior spherical Bessel coefficients cannot be determined uniquely from C^e_{nm} and S^e_{nm}. Moreover, orbit determination process does not estimate the interior spherical Bessel coefficients. Thus, we devise a mathematical reformulation and consider a series $g(\gamma)$ such that

$$\left(1 - \frac{\alpha^{i2}_{ln}}{\alpha^{2}_{l^*n}}\right) j_n(\alpha^i_{ln})\mathscr{A}^i_{lnm} = \left(\frac{g(s)}{\sum_{\gamma=1}^{\infty} g(\gamma)}\right) C^e_{nm} \tag{47}$$

where

$$s = \begin{cases} l, & \text{for } l^* = 0 \\ l - 1, & \text{for } l^* = 1 \end{cases} \tag{48}$$

Then, the summation of Eq. (47) over l, from $l = l^* + 1$, yields Eq. (46). We can consider the series $g(\gamma)$ as the weight function of the spherical harmonic coefficient C^e_{nm}; that is, a predetermined fraction of the exterior spherical harmonic coefficient is accounted for by each interior spherical Bessel coefficient. Thus, naturally, we require a convergent series for $g(\gamma)$. We can define a similar expression for $\mathscr{B}^i_{lnm}$ and get

$$\begin{cases} \mathscr{A}^i_{lnm} = \dfrac{\alpha^{i2}_{l^*n}}{(\alpha^{i2}_{l^*n} - \alpha^{i2}_{ln})\, j_n(\alpha^i_{ln})} \dfrac{g(s)}{\sum_{\gamma=1}^{\infty} g(\gamma)} C^e_{nm} \\ \mathscr{B}^i_{lnm} = \dfrac{\alpha^{i2}_{l^*n}}{(\alpha^{i2}_{l^*n} - \alpha^{i2}_{ln})\, j_n(\alpha^i_{ln})} \dfrac{g(s)}{\sum_{\gamma=1}^{\infty} g(\gamma)} S^e_{nm} \end{cases} \tag{49}$$

for $l \geq l^* + 1$. The only coefficients that are not included in Eq. (49) are $A^i_{l^*nm}$ and $B^i_{l^*nm}$, both of which are obtained from the density constraint on the boundary of the exterior Brillouin sphere (Eq. 42).

$$\begin{cases} \mathscr{A}^i_{l^*nm} = -\dfrac{1}{\alpha^{i2}_{l^*n}\, j_n(\alpha^i_{l^*n})} \displaystyle\sum_{l=l^*+1}^{\infty} \alpha^{i2}_{ln}\, j_n(\alpha^i_{ln}) \mathscr{A}^i_{lnm} \\ \mathscr{B}^i_{l^*nm} = -\dfrac{1}{\alpha^{i2}_{l^*n}\, j_n(\alpha^i_{l^*n})} \displaystyle\sum_{l=l^*+1}^{\infty} \alpha^{i2}_{ln}\, j_n(\alpha^i_{ln}) \mathscr{B}^i_{lnm} \end{cases} \tag{50}$$

Explicit expressions of Eq. (49) for $n = 0$, $n = 1$, and $n > 1$ are given as

$$\mathscr{A}^i_{l00} = \frac{\alpha^{i2}_{00}}{(\alpha^{i2}_{00} - \alpha^{i2}_{l0})\, j_0(\alpha^i_{l0})} \frac{g(l)}{\sum_{\gamma=1}^{\infty} g(\gamma)} C^e_{00} \tag{51}$$

$$\begin{cases} \mathscr{A}^i_{l1m} = \dfrac{\alpha^{i2}_{01}}{(\alpha^{i2}_{01} - \alpha^{i2}_{l1})\, j_1(\alpha^i_{l1})} \dfrac{g(l)}{\sum_{\gamma=1}^{\infty} g(\gamma)} C^e_{1m} \\ \mathscr{B}^i_{l11} = \dfrac{\alpha^{i2}_{01}}{(\alpha^{i2}_{01} - \alpha^{i2}_{l1})\, j_1(\alpha^i_{l1})} \dfrac{g(l)}{\sum_{\gamma=1}^{\infty} g(\gamma)} S^e_{11} \end{cases} \tag{52}$$

$$\begin{cases} \mathscr{A}^i_{lnm} \overset{n\geq 1}{=} \dfrac{\alpha^{i2}_{1n}}{(\alpha^{i2}_{1n} - \alpha^{i2}_{ln})\, j_n(\alpha^i_{ln})} \dfrac{g(l-1)}{\sum_{\gamma=1}^{\infty} g(\gamma)} C^e_{nm} \\ \mathscr{B}^i_{lnm} \overset{n\geq 1}{=} \dfrac{\alpha^{i2}_{1n}}{(\alpha^{i2}_{1n} - \alpha^{i2}_{ln})\, j_n(\alpha^i_{ln})} \dfrac{g(l-1)}{\sum_{\gamma=1}^{\infty} g(\gamma)} S^e_{nm} \end{cases} \tag{53}$$

We refer to this conversion between the exterior spherical harmonic coefficients and interior spherical Bessel coefficients as the analytical conversion method. The choice of the function $g(\gamma)$ is arbitrary, and Herrera-Sucarrat et al. (2013) compares the accuracy of the trajectories resulting from different weight functions. In this paper, the weight function $g(\gamma)$ is defined as

$$g(\gamma) = \frac{1}{\gamma^{10}} \tag{54}$$

which is one of the weight functions used by Herrera-Sucarrat et al. Note that the same conversion method between the interior gravity field and exterior spherical Bessel gravity field is possible. This remains of theoretical interest but has no practical usage for the spacecraft navigation purposes. Details of the analytical conversion method for the exterior spherical Bessel coefficients are given in Appendix I.4.

9 First and second-order partials of the interior spherical Bessel gravity field

In this section, we derive the first and second-order partials of the interior spherical Bessel gravity field. To do so, we define the basis function $\beta^i_{nm}(\alpha^i_{ln})$ and the surface spherical harmonic potential $\mathscr{H}_{nm}$ [in the complex number notation, as defined by Werner (2010)]:

$$\begin{cases} \beta^i_{nm}(\alpha^i_{ln}) = j_n\left(\dfrac{\alpha^i_{ln} r}{R^*_e}\right)\mathscr{H}_{nm} \\ \mathscr{H}_{nm} = P_{nm}(\sin\phi)e^{im\lambda} \end{cases} \tag{55}$$

such that

$$V^i = \frac{GM^*}{R^*_e}\sum_{l=0}^{\infty}\sum_{n=0}^{\infty}\sum_{m=0}^{n}\beta^i_{nm}(\alpha^i_{ln})\cdot\begin{bmatrix}\mathscr{A}^i_{lnm}\\ \mathscr{B}^i_{lnm}\end{bmatrix} \tag{56}$$

where i in the exponent of the exponential function e is the imaginary unit that satisfies $i^2 = -1$ and shall not be confused with the superscript for the interior quantities.

9.1 Acceleration due to the interior spherical Bessel gravity field

The acceleration is given by the first-order partial of the basis function, with appropriate multipliers. The partial derivatives of the spherical harmonic functions are thoroughly discussed by Werner (2010), Takahashi et al. (2013), and Cunningham (1970), and are omitted for space purposes. We only present the final expression of the acceleration arising from the normalized interior spherical Bessel coefficients.

$$\begin{aligned}\frac{\partial}{\partial x}\bar{\beta}^i_{nm}(\alpha^i_{ln}) &\overset{m>0}{=} -\frac{\alpha^i_{ln}x}{R^*_e r}j_{n+1}\left(\frac{\alpha^i_{ln}r}{R^*_e}\right)\bar{\mathscr{H}}_{nm} - \bar{\mathscr{F}}_1(n,m)\frac{1}{r}j_n\left(\frac{\alpha^i_{ln}r}{R^*_e}\right)\bar{\mathscr{H}}_{n-1,m+1} \\ &\quad + \bar{\mathscr{F}}_2(n,m)\frac{1}{r}j_n\left(\frac{\alpha^i_{ln}r}{R^*_e}\right)\bar{\mathscr{H}}_{n-1,m-1} \\ &\overset{m=0}{=} -\frac{\alpha^i_{ln}x}{R^*_e r}j_{n+1}\left(\frac{\alpha^i_{ln}r}{R^*_e}\right)\bar{\mathscr{H}}_{n0} - 2\bar{\mathscr{F}}_1(n,m)\frac{1}{r}j_n\left(\frac{\alpha^i_{ln}r}{R^*_e}\right)\bar{P}_{n-1,1}\begin{bmatrix}\cos\lambda\\ 0\end{bmatrix}\end{aligned} \tag{57}$$

$$\begin{aligned}\frac{\partial}{\partial y}\bar{\beta}^i_{nm}(\alpha^i_{ln}) &\overset{m>0}{=} -\frac{\alpha^i_{ln}y}{R^*_e r}j_{n+1}\left(\frac{\alpha^i_{ln}r}{R^*_e}\right)\bar{\mathscr{H}}_{nm} + \bar{\mathscr{F}}_1(n,m)\frac{1}{r}j_n\left(\frac{\alpha^i_{ln}r}{R^*_e}\right)i\bar{\mathscr{H}}_{n-1,m+1} \\ &\quad + \bar{\mathscr{F}}_2(n,m)\frac{1}{r}j_n\left(\frac{\alpha^i_{ln}r}{R^*_e}\right)i\bar{\mathscr{H}}_{n-1,m-1} \\ &\overset{m=0}{=} -\frac{\alpha^i_{ln}y}{R^*_e r}j_{n+1}\left(\frac{\alpha^i_{ln}r}{R^*_e}\right)\bar{\mathscr{H}}_{n0} - 2\bar{\mathscr{F}}_1(n,m)\frac{1}{r}j_n\left(\frac{\alpha^i_{ln}r}{R^*_e}\right)\bar{P}_{n-1,1}\begin{bmatrix}\sin\lambda\\ 0\end{bmatrix}\end{aligned} \tag{58}$$

$$\frac{\partial}{\partial z}\bar{\beta}^i_{nm}(\alpha^i_{ln}) = -\frac{\alpha^i_{ln}z}{R^*_e r}j_{n+1}\left(\frac{\alpha^i_{ln}r}{R^*_e}\right)\bar{\mathscr{H}}_{nm} + \bar{\mathscr{F}}_3(n,m)\frac{1}{r}j_n\left(\frac{\alpha^i_{ln}r}{R^*_e}\right)\bar{\mathscr{H}}_{n-1,m} \tag{59}$$

where

$$\begin{cases} \bar{\bar{\mathscr{F}}}_1(n,m) = & \dfrac{1}{2}\sqrt{\dfrac{(2-\delta_{0m})(2n+1)(n-m)!}{2(2n-1)(n-m-2)!}} \\ \bar{\bar{\mathscr{F}}}_2(n,m) = & \dfrac{1}{2}\sqrt{\dfrac{(2-\delta_{0m})(2n+1)(n+m)!}{(2-\delta_{1,m})(2n-1)(n+m-2)!}} \\ \bar{\bar{\mathscr{F}}}_3(n,m) = & \sqrt{\dfrac{(2n+1)}{(2n-1)}(n+m)(n-m)} \end{cases} \tag{60}$$

9.2 Dynamics matrix due to the interior spherical Bessel gravity field

The second-order partials, also referred to as the dynamics matrix, can be directly computed to show that

$$\nabla^2 \beta^i_{nm}(\alpha^i_{ln}) = -\frac{\alpha^{i2}_{ln}}{R^{*2}_e}\beta^i_{nm}(\alpha^i_{ln}) \tag{61}$$

Thus, Poisson's equation is satisfied. The explicit expressions of the second-order partials are given in Appendix G.3. Although the form of Eq. (61) is expected, it shows that the dynamics matrix cannot be used to propagate the state transition matrix as it does not satisfy Laplace's equation. In fact, each element of the dynamics matrix computed by the interior spherical Bessel gravity field completely differs from the actual environment between the surface of the body and the exterior Brillouin sphere (i.e., the faded gray region in Fig. 3a). The only exception is a set of interior spherical Bessel coefficients obtained via the analytical conversion method and evaluated on the boundary of the exterior Brillouin sphere, in which case the dynamics matrix conforms to Laplace's equation as the density is constrained to be zero (Eq. 41).

This result reveals a paradoxical nature of the interior spherical Bessel gravity field, where both the potential and acceleration can be modeled properly but not the dynamics matrix. One would expect to see that the second-order partial of the potential is modeled well when the potential and its first-order partials are, but this is not the case. We have yet to give a clear explanation of why there is a disconnect between the first-order and second-order partials.

The following sections entail the quantitative analysis of the performance of different types of gravity field expressions. The exterior gravity field, interior gravity field, and interior spherical Bessel gravity field are compared with the truth model of homogeneous-density polyhedral gravity field. Due to the large volume of figures, tables, and equations, two supplemental materials are attached to the paper. One document contains Appendices A and B with figures, and the other contains Appendices C through I for tables and equations.

10 Performance of the exterior gravity field

In this section, we look at the performance of the exterior gravity field in the vicinity of the body surface. We will look at two types of error distributions: cross-sectional errors and surface errors. Both error types are compared with the homogeneous-density polyhedral gravity field (Werner and Scheeres 1997), which is regarded as the truth model for the rest of the paper. For the cross-sectional errors, the data points are scattered in the xy, yz, and xz-planes. For the surface errors, the data points are on the surface of the body. The errors

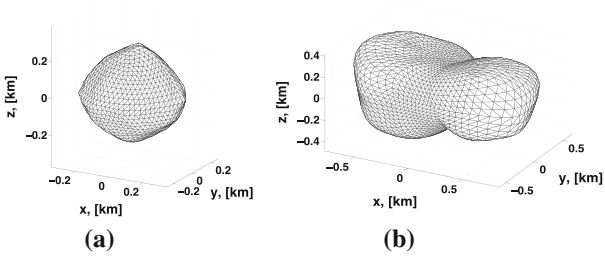

Fig. 6 Shape models of Bennu and Castalia. **a** Bennu, **b** Castalia

obtained here set the benchmark of the accuracy of the current small body gravity field modeling capabilities. The test bodies are Bennu (Fig. 6a), which is close to a spherical configuration, and Castalia (Fig. 6b) (Hudson and Ostro 1994), which is a contact binary.

For both Bennu and Castalia, the origin is placed at the center of mass of the body. The radius of the exterior Brillouin sphere (i.e., circumscribing sphere) is 0.287 km for Bennu and 0.879 km for Castalia. The closest point on the surface from the origin is 0.224 km for Bennu and 0.274 km for Castalia. The homogeneous density of the body is 0.98 g/cm^3 for Bennu and 2.1 g/cm^3 for Castalia.

10.1 Exterior gravity field around Bennu

We first look at Bennu and map the potential/acceleration errors for 0, 4, and 10-th degree exterior gravity field constructed from a homogeneously distributed body (Werner 1997). Figures A.1 and A.2 show the cross-sectional distributions of the potential/acceleration errors.[1] In both figures, the innermost black line is the cross-section of Bennu. The dotted black lines represent the exterior Brillouin sphere, within which the exterior gravity field breaks down. Each row is the degree of the exterior gravity field, and each column is the plane. The percentage errors are plotted in the log scale with base 10. That is, the plotted values (ϵ_U) are expressed by

$$\epsilon_U = \log_{10}\left[abs\left(\frac{U^e - U_{poly}}{U_{poly}}\right) \times 100\right] \tag{62}$$

As shown in Figure A.1, the magnitude of the potential errors decreases as higher-degree and higher-order terms are included, yielding a fan-like structure that protrude radially outward. The maximum potential error is on the order of several percent. The maximum acceleration error reaches ∼20 % for the zeroth-degree and ∼10 % for the 10th-degree exterior gravity field. In general, the potential is better approximated than the acceleration.

In Figure A.3, we show the potential/acceleration errors between the polyhedral gravity field and exterior gravity field on the surface of the body. Each row is the degree of the exterior gravity field, and each column is the potential/acceleration errors. The values are plotted in percentage. As with the cross-sectional error distributions, the potential is modeled better than the acceleration. The higher-degree and higher-order gravity fields yield a large number of small-scale, concentrated errors, which correspond to the fan-like structure shown in Figures A.1 and A.2. Table 1 summarizes the maximum, minimum, mean, and standard deviation of the potential/acceleration errors of the exterior gravity field on the surface of Bennu.

[1] Figure 7 shows a subset of Figures A.1 and A.2 (in Appendix A). The cross section is the xz-plane and $n = 10$.

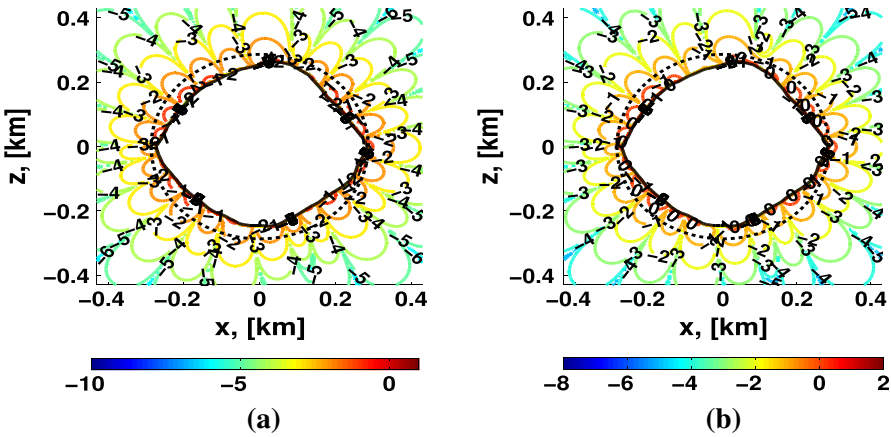

Fig. 7 Potential and acceleration errors ([log 10(%)]) in the xz-plane between the polyhedral gravity field and 10×10 exterior gravity field for Bennu.
a Potential errors, xz-plane,
b Acceleration errors, xz-plane

Table 1 Surface potential/acceleration errors (%) between the polyhedral gravity field and exterior gravity fields for Bennu

Degree (n)	Maximum	Minimum	Mean	Standard deviation
Potential				
0	3.80464	−4.23787	0.768874	1.81990
4	1.52346	−1.07433	0.0865826	0.501408
10	0.549317	−0.513510	2.30166×10^{-3}	0.139242
Acceleration				
0	19.2068	−18.4192	2.35658	6.96270
4	10.9592	−9.41072	0.747961	3.68576
10	7.03440	−6.67813	0.114995	1.87574

10.2 Exterior gravity field around Castalia

Next, we evaluate the performance of the exterior gravity field around Castalia.[2] The potential errors (Figure B.1) are significantly larger for Castalia than for Bennu due to its highly non-spherical shape. It is seen that the neck region is especially hard to characterize the gravity field environment. Near the surface of the body, >100 % errors, or even >1000 % errors, are not uncommon. The same trend is seen for the acceleration errors (Figure B.2), and the aspherical shape of the body rapidly degrades the accuracy of the exterior gravity field. The surface errors are enormous, and it is meaningless to plot them. This analysis reports the exterior gravity field's vulnerability within the exterior Brillouin sphere and that it can yield tremendously large errors (>100 %) for a body with a non-spherical shape.

[2] Figure 8 shows a subset of Figures B.1 and B.2 (in Appendix B). The cross section is the xz-plane and $n = 10$.

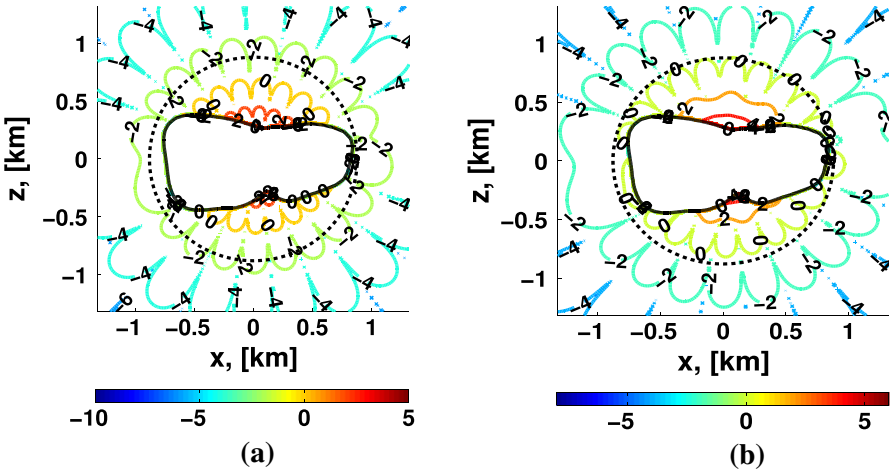

Fig. 8 Potential and acceleration errors ([log 10(%)]) in the xz-plane between the polyhedral gravity field and 10×10 exterior gravity field for Castalia. **a** Potential errors, xz-plane, **b** Acceleration errors, xz-plane

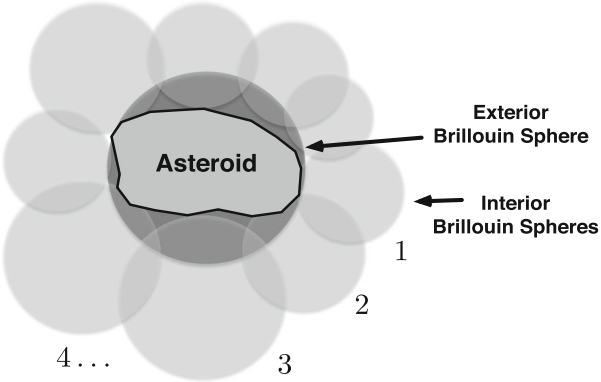

Fig. 9 Total mapping by the interior gravity fields. The *dark black sphere* in the middle is the exterior Brillouin sphere, and the *light gray spheres* surrounding the body are the interior Brillouin spheres

11 Performance of the interior gravity field

In this section, we study the performance of the interior gravity field in close proximity to the asteroid's surface. Recall that the total mapping within the exterior Brillouin sphere, including the surface, requires countless interior gravity fields as their convergence is only guaranteed up to a point on the surface (Fig. 9).

Each interior gravity field can be estimated via least-squares fit to the potential/acceleration/dynamics matrix (i.e., three source data type) computed inside the data sphere concentric with the interior coordinate center. These source data can be computed either from the exterior gravity field or polyhedral gravity field (i.e., two source gravity fields) (Takahashi et al. 2013). This method yields an interior gravity field as a complex function of the degree and order of the gravity field, the location of the interior coordinate center, source data type, size of the data sphere, and source gravity field. Furthermore, it is also possible to combine solutions from different least-squares fit to produce one set of interior gravity field coefficients (Sect. 11.2). As such, the entire search space for the optimal interior gravity

Table 2 Landing sites for Bennu and Castalia

Site #	Facet #	(x, y, z) km	(r, λ, ϕ) (km, deg., deg.)
Bennu			
1	525	(−0.200, −0.0376, 0.127)	(0.240, −169.347, 32.076)
2	929	(0.104, 0.221, 0.0430)	(0.248, 64.78, 9.978)
3	1907	(0.157, −0.101,−0.146)	(0.237, −32.697, −38.051)
Castalia			
1	574	(−0.345, −0.067, 0.370)	(0.510, −168.931, 46.44)
2	629	(0.459, 0.0235, 0.302)	(0.550, 2.937, 33.314)
3	2363	(0.0418, −0.348, −0.168)	(0.389, −83.153, −25.635)

field becomes simply too large for accurate total mapping. Thus, we will perform regional mapping instead of the total mapping.

Three landing sites are chosen for both Bennu and Castalia, and an interior gravity field is computed for each landing site (Table 2). These landing sites are arbitrarily chosen in regions where the surface is smooth so the interior Brilloin sphere can be drawn without making contacts with other parts of the body. Also, regions close to the tip are avoided, because it is of our interest to quantify the performance of the interior gravity field in regions where the exterior gravity field does not perform well.

In the following analysis, we first summarize the least-squares fit estimation for the interior spherical harmonic coefficients, then discuss the parameter space of the interior gravity field, and finally present the results of the regional mapping around Bennu and Castalia.

11.1 Conversion between an exterior gravity field and an interior gravity field

Takahashi et al. (2013) pressents a least-squares estimation technique to convert a source gravity field into an interior gravity field, and its mathematical formulation is omitted for brevity. The idea is to estimate the interior spherical harmonic coefficients that best fit the potential (plus the bias), acceleration, and/or dynamics matrix of the source gravity field for a collection of data points in the common convergence region. These data points are scattered within the data sphere, which defines a spherical boundary equal to or smaller than the interior Brillouin sphere in size. The data sphere is centered at the interior coordinate center, and its size is varied depending on the degree to which the interior gravity field is estimated and the source data type. In general, lower-degree interior spherical coefficients are estimated well when the data sphere is small. On the other hand, a large data sphere is necessary to capture the information of the higher-degree interior spherical harmonic coefficients.

11.2 Parametric space for interior gravity field estimation

In the real spacecraft rendezvous mission, only the exterior gravity field is determined through OD, and the surface gravity field is not available. Thus, the source gravity field is chosen to be the exterior gravity field. Specifically, we will use a 15×15 exterior gravity field whose spherical harmonic coefficients are generated from polyhedral integration of a constant-density body as was done in Sect. 10. Such a case represents a rather optimistic scenario where the exterior gravity field is determined to high fidelity. The actual OD solution may not contain as many higher-degree and higher-order coefficients, but this scenario will allow one to see the intrinsic powerfulness of the interior gravity field.

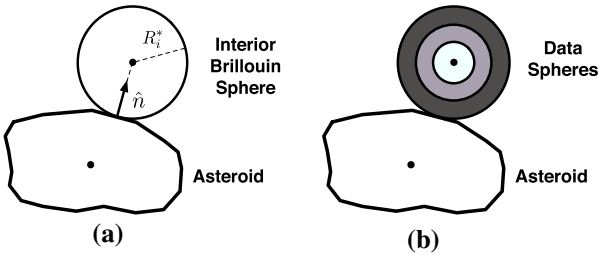

Fig. 10 Placement of the interior coordinate center and the data spheres. **a** Landing site, surface normal, and interior coordinate center, **b** data spheres

Table 3 Parameters of the estimated interior gravity fields around Bennu

Site #	R_i^* km	Degree (n)	Data type	Estimated degree (n) for each subset	Assigned degree (n) from each subset	Data sphere size w.r.t. Brillouin radius
1	1.0	30	(2, 2, 2)	(10, 25, 30)	($1 \to 5, 6 \to 20, 21 \to 30$)	(0.3, 0.8, 0.99999)
2	1.0	35	(2, 2, 2)	(10, 25, 35)	($1 \to 5, 6 \to 20, 21 \to 35$)	(0.3, 0.8, 0.99999)
3	1.0	30	(2, 2, 2)	(10, 25, 30)	($1 \to 5, 6 \to 20, 21 \to 30$)	(0.3, 0.8, 0.99999)

As alluded earlier, lower-degree interior spherical harmonics are estimated better when a small data sphere is used, and vice versa. Thus, in order to construct an interior gravity field that is accurate out to the boundary of the interior Brillouin sphere, it is often judicious to combine solutions obtained from different parametric settings. We will refer to each solution as a *subset*. For convenience, we denote the data types numerically and use 1 for the potential data, 2 for the acceleration data, and 3 for the dynamics matrix data.

The location of the landing site and the radius of the interior Brillouin sphere uniquely fix the location of the interior coordinate center. As shown in Fig. 10a, the interior coordinate center lies along the surface normal displaced by R_i^* from the landing site. Then, for a given Brillouin sphere, we have freedom to choose the degree and order of the interior gravity field which consists of multiple subsets of interior spherical harmonics, which again are estimated with varying degrees and data sphere sizes. For example, Fig. 10b shows three data spheres within an interior Brillouin sphere.

Moreover, not all the coefficients estimated for a subset needs to be assigned to the final solution. For instance, when a 10×10 gravity field is estimated, only a 5×5 gravity field can be assigned to the final solution. With as many variables as there are, the search for the optimal interior gravity field is not trivial. Therefore, an interior gravity field is estimated for each landing site by singly exploring the aforementioned parametric space. Automated search algorithm is possible in a powerful enough computing environment.

11.3 Regional mapping by interior gravity fields around Bennu

Three interior gravity fields are constructed around Bennu to perform regional mapping of its gravity field. Table 3 shows the parameters used for the least-squares fit. In Table 3, the size of the data sphere is given in ratio with respect to the radius of the interior Brillouin sphere. As shown in Table 3, each solution consists of three subsets of solutions. These parametric settings yield the 3D error distribution within the interior Brillouin spheres in Figure A.4. It is shown that all acceleration errors are less than 3 %. In order to quantify the accuracy of these interior gravity fields, the acceleration error is computed at the landing site (i.e., TAG point) with respect to the polyhedral model (i.e., the truth model). In addition, the data points

Table 4 Acceleration errors by interior gravity fields around Bennu

Site #	1	2	3
TAG point error (%)	1.123	−2.211	0.1598
Maximum error on the shell (%)	2.606	2.183	1.736
Minimum error on the shell (%)	−2.159	−2.211	−1.931
Mean error on the shell (%)	3.846×10^{-2}	5.437×10^{-4}	-6.430×10^{-2}
Standard deviation on the shell (%)	0.676	0.429	0.615

Table 5 Parameters of the estimated interior gravity fields around Castalia

Site #	R_i^* km	Degree (n)	Data type	Estimated degree (n) for each subset	Assigned degree (n) from each subset	Data sphere size w.r.t. Brillouin radius
1	2.5	30	(2, 2, 2)	(10, 20, 30)	$(1 \to 5, 6 \to 15, 16 \to 30)$	(0.3, 0.8, 0.99999)
2	2.0	35	2	35	$1 \to 35$	1
3	2.5	35	2	35	$1 \to 35$	1

are scattered on the boundary of the interior Brillouin sphere (i.e., interior Brillouin shell) in evenly spaced (20×20) grid of latitude and longitude to evaluate the maximum, minimum, mean, and standard deviation of the acceleration errors (Table 4).

As shown in Table 4, the TAG point acceleration errors are less than a few percent for all three cases, and so are the maximum/minimum errors. Note that the mean is indistinguishable from zero, and the standard deviations are less than one percent. Thus, the maximum and minimum values are outside the 3σ bounds and represent only a small fraction of all data points. This result indicates that the interior gravity field outperform the exterior gravity field by approximately an order of magnitude for Bennu.

11.4 Regional mapping by interior gravity fields around castalita

The regional mapping via interior gravity fields is also carried out around Castalia. Table 5 shows the parametric settings for the least-squares fit.

Note that for landing sites 2 and 3, their solutions are obtained solely from one data type/sphere. These settings yield the 3D error distribution shown in Figure B.3. It appears that there are only two interior gravity fields plotted, but it is an artifact of two landing sites being close to each other (i.e., site 1 and 2). The acceleration errors have increased slightly, up from ∼3 % for Bennu to ∼5 % for Castalia. This is the result of highly non-spherical shape of Castalia which makes the interior spherical harmonic coefficients estimation more difficult for Castalia than for Bennu. The quantitative performance of the regional mapping around Castalia is given in Table 6.

Table 6 shows that the maximum/minimum acceleration errors are obtained at the TAG sites. However, the acceleration errors are still on the order of several percent, which is the accuracy never achievable with the exterior gravity field, as shown in Sect. 10.2. Thus, the

Table 6 Acceleration errors by interior gravity fields around Castalia

Site #	1	2	3
TAG point error (%)	4.706	2.905	−4.075
Maximum error on the shell (%)	4.706	2.905	3.078
Minimum error on the shell (%)	−3.463	−2.903	−4.075
Mean error on the shell (%)	2.352×10^{-2}	8.911×10^{-2}	-6.946×10^{-3}
Standard deviation on the shell (%)	0.917	0.537	0.679

Table 7 Parameters for the analytical conversion of an interior spherical Bessel gravity field from an exterior gravity field

Case	Degree (n)	Power (l)
1	4	2
2	4	5
3	10	2
4	10	5
5	15	2
6	15	5

interior gravity field performs well in close proximity to the body surface (even for a highly non-spherical body) when the source data is determined with sufficient accuracy.

12 Performance of the interior spherical Bessel gravity field

In this section, we investigate the performance of the interior spherical Bessel gravity field. We will test two cases where the interior spherical Bessel coefficients are analytically converted from the exterior gravity field by enforcing the boundary conditions (Sect. 8) and they are estimated via least-squares fit as was done for the interior gravity field (Sect. 11).

12.1 Analytical conversion method

First, we convert the exterior spherical harmonic coefficients into the interior spherical Bessel coefficients by analytical conversion method (Eqs. 50 through 53). The only parameters we change are the degree and power of the interior spherical Bessel gravity field. We will test six cases in Table 7.

Note that, in the actual spacecraft mission, the higher-degree ($n \geq 10$) exterior gravity field may not be determined. Nonetheless, the parameters in Table 7 are explored to study the intrinsic capabilities of the analytically converted interior spherical Bessel gravity field.

12.1.1 Performance of the analytically converted interior spherical Bessel gravity field around Bennu

Figures A.5 and A.6 show the surface potential/acceleration errors of Bennu for case 1 through 6.[3] In both figures, the higher-degree interior spherical Bessel gravity field yields

[3] The acceleration error plot for case 1 for Bennu is shown in Fig. 11. The identical plot is given in Figure A.6.

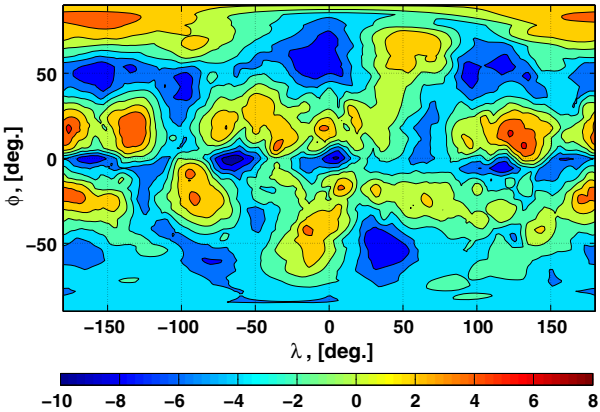

Fig. 11 Surface acceleration errors (%) between the polyhedral gravity field and analytically converted interior spherical Bessel gravity field for case 1 ($n = 4$ and $l = 2$) for Bennu

Table 8 Surface potential/acceleration errors (%) between the polyhedral gravity field and analytically converted interior spherical Bessel gravity fields: case 1 through case 6 for Bennu

Degree (n)	Power (l)	Maximum	Minimum	Mean	Standard deviation
Potential					
4	2	1.30730	−1.10122	-8.09664×10^{-4}	0.458908
4	5	1.30726	−1.10119	-7.84872×10^{-4}	0.458883
10	2	0.384995	−0.319545	−0.0708242	0.104228
10	5	0.384959	−0.319398	−0.0707926	0.104222
15	2	0.210780	−0.256909	−0.0698102	0.0747787
15	5	0.210769	−0.256911	−0.0697783	0.0747769
Acceleration					
4	2	6.60441	−9.44079	−1.37583	2.76404
4	5	6.60303	−9.44080	−1.37548	2.76361
10	2	4.21681	−5.15143	−1.65999	1.43883
10	5	4.21610	−5.15071	−1.65949	1.43890
15	2	3.35731	−4.91601	−1.64271	1.32577
15	5	3.35682	−4.91594	−1.64220	1.32589

smaller potential/acceleration errors, but there is no significant change for different powers. All acceleration errors are within 10 % on the surface of Bennu (Table 8).

12.1.2 Performance of the analytically converted interior spherical Bessel gravity field around Castalia

Figures B.4 and B.5 show the surface potential/acceleration errors of Castalia for case 1 through 6.[4] Both plots show significantly larger errors than Bennu. However, the errors are contained under 10 % for potential and 30 % for acceleration. It is a significant improvement from the exterior gravity field, which frequently yields >100 % errors on the surface of the

[4] The acceleration error plot for case 1 for Castalia is shown in Fig. 12. The identical plot is given in Figure B.5.

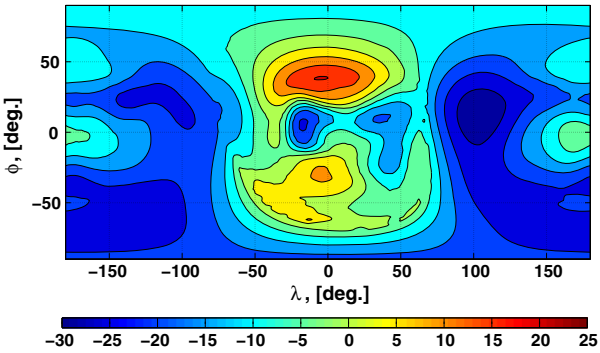

Fig. 12 Surface acceleration errors (%) between the polyhedral gravity field and analytically converted interior spherical Bessel gravity field for case 1 ($n = 4$ and $l = 2$) for Castalia

Table 9 Surface potential/acceleration errors (%) between the polyhedral gravity field and analytically converted interior spherical Bessel gravity fields: case 1 through case 6 for Castalia

Degree (n)	Power (l)	Maximum	Minimum	Mean	Standard deviation
Potential					
4	2	8.55932	−4.38073	−0.304808	2.01725
4	5	8.55508	−4.37939	−0.301064	2.01755
10	2	4.59364	−3.53261	−0.462649	1.59061
10	5	4.59430	−3.53079	−0.458757	1.59152
15	2	4.62814	−3.47930	−0.464882	1.58656
15	5	4.62866	−3.47724	−0.460992e	1.58748
Acceleration					
4	2	20.1551	−28.3260	−10.5150	9.18088
4	5	20.1077	−28.3173	−10.5188	9.17073
10	2	25.0558	−27.9169	−10.4564	7.71477
10	5	25.0286	−27.9085	−10.4591	7.70785
15	2	21.8928	−27.6136	−10.5238	7.51102
15	5	21.8671	−27.6063	−10.5264	7.50418

body. Notice that, compared to Figures A.5 and A.6, larger errors are spread out more widely in Figures B.4 and B.5.

Table 9 summarizes the maximum, minimum, mean, and standard deviation of the potential/acceleration errors of the analytically converted interior spherical Bessel gravity fields on the surface of Castalia.

12.2 Fitting to the polyhedral gravity field acceleration

In this section, instead of fitting the interior spherical Bessel coefficients to the exterior spherical harmonic coefficients, we estimate them via the least-squares fit to the uniform-density polyhedral gravity field. Such a conversion represents the ideal scenario where we know the density distribution of the body and have the true gravity field available. The estimated interior spherical Bessel gravity field greatly facilitate the potential/acceleration computation and reduce the overall computation time compared to the polyhedral integration.

The interior spherical Bessel coefficients ($\mathscr{A}^i_{lnm}$, $\mathscr{B}^i_{lnm}$) are estimated the same way the interior spherical harmonic coefficients (C^i_{nm}, S^i_{nm}) are estimated from the exterior gravity field (C^e_{nm}, S^e_{nm}) as was done in Sect. 11. Recall that the interior gravity field is fit to the potential/acceleration/dynamics matrix of the exterior gravity field in a least-squares sense. Here, as the dynamics matrix does not satisfy Laplace's equation, the potential and acceleration are the only source data. In the following, the methodology of the least-squares fit and the performance of the estimated interior spherical Bessel gravity fields are discussed. We will first show the general trend of the least-squares fit solution and commence the search for the optimal interior spherical Bessel gravity field.

12.2.1 Least-squares conversion of the interior spherical Bessel gravity field

The least-squares estimation of the interior spherical Bessel coefficients is carried out in the same manner as that of the interior spherical harmonic coefficients (Sect. 11.1). The state vector consists of the interior spherical Bessel coefficients ordered in the following manner.

$$
\begin{aligned}
[\tilde{\mathscr{A}}^i_{lnm}] = \Big[& \mathscr{A}^i_{000}, \mathscr{A}^i_{010}, \mathscr{A}^i_{011}, \mathscr{B}^i_{011}, && l = 0 \\
& \mathscr{A}^i_{100}, \mathscr{A}^i_{110}, \mathscr{A}^i_{111}, \mathscr{B}^i_{111}, \mathscr{A}^i_{120}, \mathscr{A}^i_{121}, \mathscr{B}^i_{121}, \mathscr{A}^i_{122}, \mathscr{B}^i_{122}, \mathscr{A}^i_{130}, \cdots && l = 1 \\
& \mathscr{A}^i_{200}, \mathscr{A}^i_{210}, \mathscr{A}^i_{211}, \mathscr{B}^i_{211}, \mathscr{A}^i_{220}, \mathscr{A}^i_{221}, \mathscr{B}^i_{221}, \mathscr{A}^i_{222}, \mathscr{B}^i_{222}, \mathscr{A}^i_{230}, \cdots && l = 2 \\
& \cdots, && \vdots \\
& \mathscr{A}^i_{l00}, \mathscr{A}^i_{l10}, \mathscr{A}^i_{l11}, \mathscr{B}^i_{l11}, \mathscr{A}^i_{l20}, , \mathscr{A}^i_{l21}, \mathscr{B}^i_{l21}, \cdots\cdots, \mathscr{B}^i_{lnn} \Big] && l = l_{max}
\end{aligned}
\tag{63}
$$

which consists of $l(n+1)^2 + 4$ coefficients. Notice that only the zeroth and the first-degree coefficients are estimated when $l = 0$. This is because the higher-degree and higher-order terms are all zero by definition for the zeroth power, as mentioned in Sect. 7.

The objective here is to match the potential/acceleration given by the polyhedral gravity field and interior spherical Bessel gravity field. We only derive equations for the acceleration fitting, but the potential fitting can be achieved by simple substitution. The cost function is defined as

$$
J_{\mathscr{B}} = \frac{1}{2} \left([\mathscr{Q}^i_{lnm}][\tilde{\mathscr{A}}^i_{lnm}] - \frac{\partial U}{\partial \mathbf{r}} \right)^T W_{\mathscr{B}} \left([\mathscr{Q}^i_{lnm}][\tilde{\mathscr{A}}^i_{lnm}] - \frac{\partial U}{\partial \mathbf{r}} \right) \tag{64}
$$

where $W_{\mathscr{B}}$ is the weighting matrix set to be the identity matrix, and $[\mathscr{Q}^i_{lnm}]$ is the partial of acceleration with respect to each interior spherical Bessel coefficient. Therefore, the dimension of $[\mathscr{Q}^i_{lnm}]$ is $[3 \times \{l(n+1)^2 + 4\}]$. The components of $[\mathscr{Q}^i_{lnm}]$ are listed in Appendix G.4. $\partial U / \partial \mathbf{r}$ is the acceleration due to the source gravity field, which, in our case, is the polyhedral gravity field. The cost function is minimized with respect to the interior spherical Bessel coefficients $[\tilde{\mathscr{A}}^i_{lnm}]$ to yield the normal equation

$$
[\tilde{\mathscr{A}}^i_{lnm}] = \left([\mathscr{Q}^i_{lnm}]^T W_{\mathscr{B}} [\mathscr{Q}^i_{lnm}] \right)^{-1} \left\{ [\mathscr{Q}^i_{lnm}]^T W_{\mathscr{B}} \left(\frac{\partial U}{\partial \mathbf{r}} \right) \right\} \tag{65}
$$

The variance-covariance matrix is accumulated with a square-root information algorithm (Tapley et al. 2004) because it ensures that we can invert this matrix even if the number of the estimated parameters is large, or there is little sensitivity to the data. Small sensitivity is usually observed for the higher-degree, higher-order, and higher-power interior spherical Bessel coefficients. As a baseline, the square-root information algorithm is encouraged when the power of the estimated interior spherical Bessel coefficients is larger than or equal to 5.

Table 10 Least-squares fit parameters of the interior spherical Bessel gravity field estimation

Case	Degree (n)	Power (l)	Data
1	5	2	Acceleration
2	5	5	Acceleration
3	10	2	Acceleration
4	10	5	Acceleration
5	15	2	Acceleration
6	15	5	Acceleration

In Eq. (65), the acceleration at each data point gives three components. That is, the number of the data points N_{Data} has to satisfy the condition $3N_{Data} \geq l(n+1)^2 + 4$ in order to construct a full rank system. We can also use Eq. (65) to estimate the normalized interior spherical Bessel coefficients by substituting the normalized components for $[\tilde{\mathscr{A}}^i_{lnm}]$ and $[\mathscr{Q}^i_{lnm}]$. Note that a similar least-squares fit to the potential data is also possible, and the base gravity field model needs not be the polyhedral gravity field; the same methodology applies to the mascon model, the interior gravity field, and any other gravity field models that have an overlapping convergence region with the interior spherical Bessel gravity field.

Table 10 shows the parameters of the interior spherical Bessel gravity field estimation. In Table 10, only the acceleration is used as data because the preliminary analysis showed that the estimated interior spherical Bessel gravity field is more accurate when fit to the acceleration than to the potential. For all cases, we scatter the data points in evenly-spaced $(30 \times 30 \times 10)$ grid in latitude, longitude, and radial distance outward from the surface of the body to the boundary of the exterior Brillouin sphere. That is, the data points reside between the surface of the body and the exterior Brillouin sphere. The ratio of the size of the data sphere to that of the exterior Brillouin sphere is 0.999.

12.2.2 General performance of the fitted interior spherical Bessel gravity field around Bennu

Figures A.7 and A.8 show the surface potential/acceleration errors between the polyhedral and estimated (least-squares fit) interior spherical Bessel gravity fields for Bennu. In general, the potential is better estimated than the acceleration. Also, a higher-degree gravity field produces smaller errors. However, inspection of Table 11 indicates that there exists an optimal power l for the least-squares solution, and a large l does not necessarily produce smaller errors. For Bennu, the performance of the least-squares fit is comparable to the analytical conversion method.

12.2.3 General performance of the fitted interior spherical Bessel gravity field around Castalia

Figures B.6 and B.7 show the surface potential/acceleration errors between the polyhedral and estimated (least-squares fit) interior spherical Bessel gravity fields for Castalia. Notice the large variations in the accuracy of the solution between each case. This result is attributed to the highly non-spherical shape of Castalia. Its irregular shape necessitates accurate estimation of the higher-degree, higher-order, higher-power coefficients, whose information content resides in the close proximity to the surface, or rather, the concave neck region closest to

Table 11 Surface potential/acceleration errors (%) between the polyhedral gravity field and estimated (least-squares fit) interior spherical Bessel gravity fields: case 1 through case 6 for Bennu

Degree (n)	Power (l)	Maximum	Minimum	Mean	Standard deviation
Potential					
5	2	1.12686	−0.976124	−0.0203532	0.303438
5	5	0.838613	−1.14662	−0.0523238	0.295245
10	2	0.278297	−0.407028	−0.0268360	0.0714052
10	5	0.240126	−0.375800	6.68248×10^{-4}	0.0637953
15	2	0.192670	−0.258007	−0.0541950	0.0400404
15	5	0.260357	−0.219223	-5.08978×10^{-5}	0.0330392
Acceleration					
5	2	4.15387	−9.68197	−1.57927	2.04220
5	5	5.01853	−9.30806	−1.83312	1.62047
10	2	3.77595	−5.98568	−0.490040	1.13909
10	5	2.77834	−5.88321	−0.705962	0.906725
15	2	4.47100	−4.89808	−0.335766	0.948939
15	5	6.75528	−7.44448	−0.352836	0.958916

Table 12 Surface potential/acceleration errors (%) between the polyhedral gravity field and estimated (least-squares fit) interior spherical Bessel gravity fields: case 1 through case 6 for Castalia

Degree (n)	Power (l)	Maximum	Minimum	Mean	Standard deviation
Potential					
5	2	1.86773	−4.84572	−0.295941	0.747621
5	5	2.00176	−4.17350	−0.0664875	0.596186
10	2	0.776255	−1.74959	−0.317971	0.430355
10	5	0.5.28400	−0.738369	5.55394×10^{-3}	0.106925
15	2	0.814651	−1.51113	−0.314963	0.415563
15	5	0.525769	−0.410197	4.96216×10^{-3}	0.0499295
Acceleration					
5	2	6.72306	−20.9619	−7.16324	4.33379
5	5	9.03643	−20.5132	−3.20296	4.47056
10	2	8.69943	−18.6340	−5.50982	4.30593
10	5	5.98371	−11.5945	−0.902768	1.82682
15	2	9.63535	−18.7409	−5.17161	4.48272
15	5	11.5996	−8.06015	−0.327993	1.46124

the origin. As with Bennu, it is evident that there exists an optimal interior spherical Bessel gravity field (Table 12). Thus, we will search for such a solution in the next section.

12.3 Optimal interior spherical Bessel gravity field via least-squares fit

Now that the general performance of the interior spherical Bessel gravity field is studied, it became apparent that there exists an optimal interior spherical Bessel gravity field of some

Table 13 Search space for the optimal interior spherical Bessel gravity field

Degree (n)	Power (l)	Source data	Combination type
5, 8, 10, 12, 15, 18, 20	2, 5, 8, 10	Potential, acceleration, Potential and acceleration	Degree-wise, Power-wise

degree n and some power l. We search for such a gravity field iteratively for particular sets of search space in degree, power, source data type, and combination type. Our algorithm works as follows. First we estimate interior spherical Bessel gravity fields from only one source data type (either potential or acceleration) for a given degree and power. The source gravity field is the polyhedral gravity field with a homogeneous density. These solutions are referred to as the direct solutions. Then, after all direct solutions are obtained, these solutions are combined to check whether the combined solutions yield better accuracy than the direct ones. Note that the solutions from the same source data are not combined. That is, we combine the solutions estimated from the potential data with those estimated from the acceleration data. Then, the combined solutions are formulated either degree-wise or power-wise. The degree-wise combination yields an interior spherical Bessel gravity field assigning certain degree gravity fields from one solution and the rest from another, both for the full power. The power-wise combination yields an interior spherical Bessel gravity field assigning certain power gravity fields from one solution and the rest from another, both for the full degree. The search space of the parameters is shown in Table 13.

The parameter space in Table 13 yields 28 direct solutions and 9,660 combined solutions. For each solution, the potential, acceleration, and acceleration gradient errors (angle between the accelerations given by the polyhedral and estimated interior spherical Bessel gravity field) are computed on the surface of the body in (20×20) grid in latitude and longitude. Then, the maximum, minimum, mean, and standard deviation of the potential/acceleration/acceleration gradient errors are computed for each solution.

12.3.1 Performance of the optimally fitted interior spherical Bessel gravity field for Bennu

We present the performance of the optimal interior spherical Bessel gravity field for Bennu. When the parameter space is explored, the minimum value in the absolute value (i.e., $min(abs(value))$) is output for each error type, which yields Table 14.

Table 14 gives one a pointer to the optimal interior spherical Bessel gravity field. Each value corresponds to different solution type and degree/power of the interior spherical Bessel gravity field. The degree and power are omitted to avoid the clutter. Of all four error types shown in Table 14, the maximum and minimum values do not constitute reliable criteria as these values come from one particular data point on the surface. In fact, the corresponding solutions tend to have large errors for other data points as well. On the contrary, the mean is representative of all data points, but large errors in opposite signs can average out. We observed many such cases as well. Thus, we select the solution with the smallest standard deviation in order to find a solution that yields consistently small errors. Specifically, we choose the solution with the minimum standard deviation in the acceleration errors, as preliminary analysis (Sect. 12.2) showed that the acceleration is harder to fit than the potential. The optimal solution for Bennu is given by the $20 \times 20 \times 2$ interior spherical Bessel gravity field obtained directly from the acceleration data.

Table 14 Search results for the optimal interior spherical Bessel gravity field for Bennu

Solution type	Maximum	Minimum	Mean	Standard deviation
Potential errors (%)				
Potential	1.19384e−01	2.43402e−01	1.00365e−02	5.18963e−02
Acceleration	2.89987e−02	7.96367e−02	1.68716e−03	2.16761e−02
Potential → acceleration, degree-wise	8.64134e−02	8.80883e−02	2.02419e−05	3.28350e−02
Potential → acceleration, power-wise	8.91628e−02	7.96367e−02	5.28855e−04	2.16761e−02
Acceleration → potential, degree-wise	1.39828e−01	1.94247e−01	7.63359e−04	5.89729e−02
Acceleration → potential, power-wise	1.45387e−01	2.74382e−01	5.60008e−03	5.76799e−02
Acceleration errors (%)				
Potential	1.94184e+00	6.58638e+00	1.58734e−02	1.33255e+00
Acceleration	2.31592e+00	2.42479e+00	1.97550e−01	7.97654e−01
Potential → acceleration, degree-wise	7.48083e−02	6.06490e−01	9.50240e−03	9.30130e−01
Potential → acceleration, power-wise	2.31592e+00	3.59089e+00	2.21346e−02	8.72401e−01
Acceleration → potential, degree-wise	1.94414e+00	3.36187e−02	1.52033e−04	1.01990e+00
Acceleration → potential, power-wise	7.69208e+00	1.14874e+01	3.07032e−01	3.05316e+00
Acceleration gradient errors (deg.)				
Potential	2.07197e+00	8.72756e−03	5.18788e−01	3.58804e−01
Acceleration	1.02556e+00	7.22915e−03	2.46312e−01	1.83237e−01
Potential → acceleration, degree-wise	1.02696e+00	1.03248e−03	2.88262e−01	1.84794e−01
Potential → acceleration, power-wise	1.02556e+00	7.22918e−03	2.46312e−01	1.88764e−01
Acceleration → potential, degree-wise	1.85724e+00	2.26463e−03	5.26049e−01	3.22479e−01
Acceleration → potential, power-wise	2.35684e+00	6.72147e−03	6.01131e−01	4.15580e−01

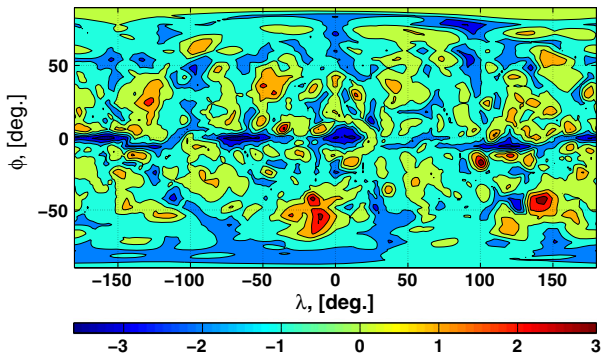

Fig. 13 Surface acceleration errors (%) between the polyhedral gravity field and optimal interior spherical Bessel gravity field for Bennu

Figure A.9 shows the surface potential/acceleration errors between the polyhedral gravity field and optimal interior spherical Bessel gravity field.[5] The magnitude of the resulting maximum/minimum surface errors is not much different from those generated by the analytically converted interior spherical Bessel gravity field (Sect. 12.1.1). Thus, for a body as spherical as Bennu, the analytical conversion works sufficiently well.

Figure A.10 shows the cross-sectional distribution of the potential/acceleration errors between the polyhedral gravity field and the combination of the exterior and optimal interior

[5] The acceleration errors are shown in Fig. 13.

Table 15 Search results for the optimal interior spherical Bessel gravity field for Castalia

Solution type	Maximum	Minimum	Mean	Standard deviation
Potential errors (%)				
Potential	2.68023e−01	4.63081e−01	1.90473e−03	1.12030e−01
Acceleration	1.87689e−01	1.26295e−01	2.59914e−03	3.02350e−02
Potential → acceleration, degree-wise	2.53351e−01	4.85438e−01	4.90898e−04	1.20796e−01
Potential → acceleration, power-wise	1.87689e−01	1.26295e−01	2.61616e−04	3.02350e−02
Acceleration → potential, degree-wise	3.01624e−01	3.57605e−01	4.73147e−04	8.02895e−02
Acceleration → potential, power-wise	4.37317e−01	4.63081e−01	1.90473e−03	1.12030e−01
Acceleration errors (%)				
Potential	7.25948e−01	1.06465e+01	3.45349e−01	2.74251e+00
Acceleration	2.81395e+00	5.04134e+00	1.70893e−01	1.17291e+00
Potential → acceleration, degree-wise	1.78024e−02	5.85643e−01	4.88040e−03	2.73543e+00
Potential → acceleration, power-wise	2.81395e+00	5.04134e+00	2.51816e−02	1.17291e+00
Acceleration → potential, degree-wise	3.05756e+00	2.80896e+00	3.86657e−02	1.43766e+00
Acceleration → potential, power-wise	4.20644e+00	5.55305e+00	2.86288e−01	2.74251e+00
Acceleration gradient errors (deg.)				
Potential	4.08312e+00	6.08356e−03	5.43863e−01	5.64596e−01
Acceleration	1.39947e+00	1.84591e−03	2.03320e−01	2.45588e−01
Potential → acceleration, degree-wise	3.30978e+00	1.58088e−03	5.91717e−01	5.55263e−01
Potential → acceleration, power-wise	1.39947e+00	1.84591e−03	2.03320e−01	2.45588e−01
Acceleration → potential, degree-wise	2.46718e+00	8.14447e−03	4.89220e−01	4.32567e−01
Acceleration → potential, power-wise	4.06904e+00	6.08356e−03	5.43863e−01	5.64596e−01

spherical Bessel gravity fields, produced in a similar manner to Figures A.1, A.2, B.1, and B.2. The errors are computed with respect to the exterior gravity field outside the exterior Brillouin sphere and with respect to the optimal interior gravity field inside it. As shown, both the potential and acceleration are modeled accurately.

12.3.2 Performance of the optimally fitted interior spherical Bessel gravity field for Castalia

We explore the same parameter space in Table 13 in order to find the optimal interior spherical Bessel gravity field for Castalia. Table 15 is obtained when we compute the potential/acceleration/acceleration gradient errors in (20×20) grid in latitude and longitude on the surface of the body.

The optimal solution is given by the $18 \times 18 \times 5$ interior spherical Bessel gravity field obtained by the direct solution from the acceleration data or by the power-wise combination of the potential/acceleration data ($l = 0 \rightarrow 2$ from the potential data and $l = 3 \rightarrow 5$ from the acceleration). For convenience, we use the direct acceleration solution to generate the error plots.

Figure B.8 shows the surface potential/acceleration errors between the polyhedral gravity field and optimal interior spherical Bessel gravity field for Castalia.[6] Notice the significant reduction in surface potential/acceleration errors from the exterior gravity field or analytically

[6] The acceleration errors are shown in Fig. 14.

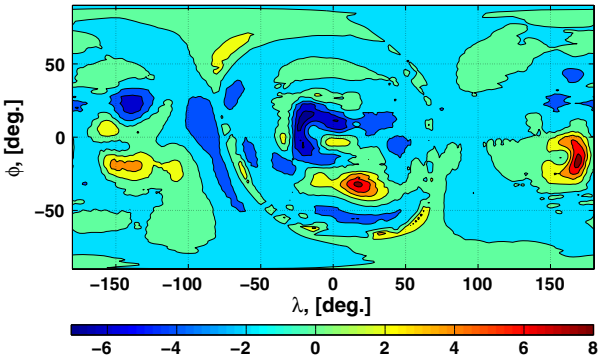

Fig. 14 Surface acceleration errors (%) between the polyhedral gravity field and optimal interior spherical Bessel gravity field for Castalia

converted interior spherical Bessel gravity field. Often the potential and acceleration errors are larger than 100 % for the exterior gravity field. However, the potential errors are reduced to less than 1 %, and the acceleration errors are less than 8 % for the optimal interior spherical Bessel potential. The same order of accuracy cannot be achieved by the analytical conversion method. It is important to note that the largest errors are contained in small regions on the surface, and we do not see widespread, large error distribution shown in the analytically converted solutions (Figures B.4 and B.5). This result shows the inherent powerfulness of the interior spherical Bessel gravity field.

It is worthwhile to note that the errors of the optimal solutions are on the same order for both Bennu and Castalia, showing no clear evidence of modeling difficulty for both spheroidal and highly non-spherical bodies. Figure B.9 shows the cross-sectional distribution of the potential/acceleration errors between the polyhedral gravity field and combination of the exterior and optimal interior spherical Bessel gravity fields for Castalia.

13 Discussions and recommendations

We have evaluated the gravity field environment around Bennu and Castalia near their surface using the exterior spherical harmonic gravity field, interior spherical harmonic gravity field, and interior spherical Bessel gravity field. One body is nearly spherical and the other a two-lobe configuration, representing two extremes of the shapes that exist for small bodies. The three types of gravity field expansions are compared against the polyhedral gravity field model constructed from a homogeneously distributed body.

The exterior gravity field performs with moderate accuracy around Bennu yielding a few percent error for potential and $<10\,\%$ error for acceleration for a 4×4 expansion on the surface. It is shown that the higher-degree and higher-order terms further reduce the surface gravity errors. However, the accuracy of the exterior gravity field rapidly deteriorates when the body deviates farther and farther from a spherical shape. For Castalia, the potential and acceleration errors exceed well over 100 % even for a 10×10 expansion. As the exterior gravity field does not converge within the exterior Brillouin sphere and there is no guarantee that it approximates the surface gravity field well for other nearly spherical body than Bennu, the exterior gravity field should never be used to model the gravitation near the surface of the body.

The interior gravity field performs well, on the order of a few percent acceleration error, to map out the regional space of the surface gravity field for both Bennu and Castalia. One drawback is that the total mapping requires considerable amount of time to optimize the

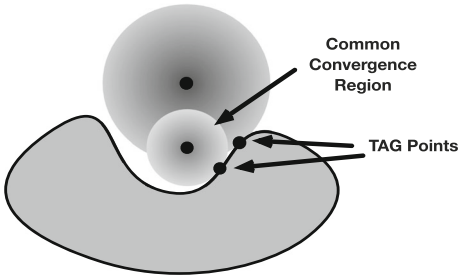

Fig. 15 Rolling interior Brillouin spheres on the surface

solution. However, this does not pose a problem when designing a trajectory/navigating a spacecraft for a particular TAG point on the surface. Although many higher-degree and higher-order terms are generally needed for the interior gravity field than the exterior gravity field and adds to the computation time, the benefit of improved accuracy is tremendous. In fact, the interior gravity field is the most computationally efficient method to characterize the surface gravity field.

While the interior gravity field is a very powerful formulation, we provide two caveats. Firstly, one must be careful with the accuracy of the source gravity field and the topology of the body's surface. In this paper, the source gravity field for the least-squares fit is a 15×15 exterior gravity field for both Bennu and Castalia. It is often extremely challenging to obtain such a high-degree solution from OD for small bodies. Thus, the performance of the interior gravity shall be evaluated on a case-by-case basis. Secondly, the surface topology of the body may prohibit one from using the interior gravity field in severely concave regions. Such a region can be mapped by the interior gravity field if we estimate a set of interior spherical harmonic coefficients by least-squares fit to an already existing interior gravity field (Fig. 15). However, the idea of *rolling* interior gravity fields is time-consuming, and it is expected that the optimization requires laborious work.

The interior spherical Bessel gravity field is obtained either by enforcing the boundary conditions or by fitting to the potential/acceleration data given from the polyhedral/interior gravity fields. As the interior gravity field fitting requires the total mapping, we only performed the polyhedral gravity field fitting in this paper. The general trends of the analytically converted solutions and the fitted solutions are presented, and the optimally fitted solutions are also given. The results show that the analytical conversion method and the fitting algorithm perform similarly for Bennu, yielding $<0.3\,\%$ potential error and $<5\,\%$ acceleration error. Both methods yield slightly less accuracy than the interior gravity field. The analytical conversion method for Castalia yields $<5\,\%$ potential error and $<20\,\%$ acceleration error. This is a significant improvement from the exterior gravity field for which $>100\,\%$ potential/acceleration errors are not uncommon. It is worthwhile to note that the analytical conversion method does not require rigorous tuning of the degree/power of the interior spherical Bessel gravity field. As a baseline, 5th-power gravity field produces moderate accuracy for any degree n. The fitted solution yields $<0.5\,\%$ potential errors and $<8\,\%$ acceleration errors on the surface of Castalia, with majority of the large errors concentrated in small regions scattered around the body. Comparison of Figure B.5 and Figure B.9 reveals that the regions with large errors are scattered in small patches when the least-squares fit is performed, while the analytical conversion method distributes the large errors on a large scale. Thus, if the surface gravity field is available (e.g., the density distribution is known for polyhedral gravity field), the least-squares fit yields an accurate interior spherical Bessel gravity field. Or, alternatively, the total mapping of the interior gravity fields can be used to produce

an accurate interior spherical Bessel gravity field, which is reiterated to be computationally expensive. For both the analytical conversion method and the least-squares fit solution, one advantage of the interior spherical Bessel gravity field is that its convergence is guaranteed anywhere inside the exterior Brillouin sphere, and the total mapping is attained from its formulation. Thus, the interior spherical Bessel gravity field can be a useful tool, for example, when analyzing the gravity anomaly for scientific purposes. Furthermore, it may find its use in geodesy to improve the knowledge of the transport of the atmosphere and ocean tides, as the outer edge of the atmosphere defines the Brillouin sphere of the Earth.

The overall performance of the exterior, interior, and interior spherical Bessel gravity fields shows that the interior gravity field is most suitable for regional mapping purposes and the interior spherical Bessel gravity field for total mapping. One caveat here is that both gravity fields do not perform well when the source gravity field does not attain sufficient accuracy, which heavily depends on the accuracy of the OD solution that varies from one body to another. Thus, a case by case analysis is needed to evaluate which method performs with desired accuracy. If only the lower-degree exterior spherical harmonic coefficients ($n < 10$) are obtained, it is recommended that the analytically converted interior spherical Bessel gravity field be used as it is likely that the fitted interior gravity field is not accurate enough for either regional mapping or total mapping.

14 Conclusions

In this paper, we investigated Poisson's equation in the form of Helmholtz's equation to seek a solution to the null space of the exterior/interior gravity fields. In fact, the outcome is that there exist two solutions that are mirror images of each other, just as the exterior and interior gravity fields are the mirror images of each other, that are named the interior/exterior spherical Bessel gravity fields. These gravity fields are derived from similar sets of spherical harmonic coefficients with the basis function expressed via the spherical Bessel function. The interior spherical Bessel gravity field complements the solution space of the exterior gravity field, and the exterior spherical Bessel gravity field complements the solution space of the interior gravity field.

We have discussed the analytical conversion method between the exterior gravity field and interior spherical Bessel gravity field by imposing the boundary condition. In addition, we estimated the interior spherical Bessel coefficients via least-squares fit to the polyhedral gravity field. Comparisons are made among four types of gravity field solutions: exterior gravity field, interior gravity field, interior spherical Bessel gravity field converted from the exterior gravity field, and that estimated via least-squares fit to the polyhedral gravity field. All errors are computed with respect to the polyhedral gravity field of homogeneous density.

The results show that the exterior gravity field performs with $<20\,\%$ acceleration error on the surface of Bennu, but as the body takes on more concavity, the errors grow exponentially ($>100\,\%$ for Castalia). The interior gravity fields constructed for each of three landing sites of Bennu and Castalia perform with $<5\,\%$ acceleration error. The analytically converted interior spherical Bessel gravity field performs with $<10\,\%$ acceleration error for Bennu and $<30\,\%$ error for Castalia. When the interior spherical Bessel coefficients are estimated via least-squares fit to the polyhedral gravity field, the optimal solution yields the acceleration errors on the order of $<5\,\%$ for Bennu and $<10\,\%$ for Castalia.

Recommendations are given based on the performance of the gravity fields analyzed in this paper. It is concluded that the interior gravity field is most suitable for regional mapping that is used for the trajectory design of a TAG point, though it is necessary to have sufficiently

accurate source gravity field for this purpose. If the OD solution yields only the lower-degree exterior gravity field, it is recommended to perform the total mapping via analytical conversion of the interior spherical Bessel gravity field, irrespective of the body's shape. The possibility of the interior spherical Bessel gravity field is not limited only to small body navigation, and it may extend to the field of geodesy.

Acknowledgments This research was supported by NASA's OSIRIS-REx New Frontiers mission through grant NNM10AA11C.

References

Abramowitz, M., Stegun, I.A. (eds.): Handbook of Mathematical Functions with Formulas, Graphs, and Mathematical Tables, chap. 9, 10. U.S. Department of Commerce and Knovel Library (online), 10th ed. (1972)

Allen, A.J., Palmer, P.L., Papaloizou, J.: A conservative numerical technique for collisionless dynamical systems: comparision of the radial and circular orbit instabilities. Mon. Not. R. Astron. Soc. **242**, 576–594 (1992)

Arfken, G.: Mathematical Methods for Physicists, chap. 9, 11, 12, 3rd edn. Academic Press Inc, NY (1985)

Brillouin, M.: Equations aux Dériveées partielles du 2e ordre. Domaines à connexion multiple. Fonctions sphériques non antipodes. Annales De L'Institut H. Poincaré **4**(2), 173–206 (1933)

Cangahuala, L.A.: Augmentations to the Polyhedral Gravity Model to Facilitate Small Body Navigation. American Astronomical Society, Washington DC (2005)

Cunningham, L.E.: On the computation of the spherical harmonic terms needed during the numerical integration of the orbital motion of an artificial satellite. Celest. Mech. **2**, 207–216 (1970)

Gottlieb, P.: Estimation of local lunar gravity features. Radio Sci. **5**(2), 301–312 (1970)

Hanna, J.R., Rowland, J.H.: Fourier Series, Transforms, and Boundary Value Problems, chap. 1, 2, 5, 6, 2nd edn. A Wiley-Interscience Publication, London (1990)

Herrera-Sucarrat, E., Palmer, P., Roberts, R.: Modeling the gravitational potential of a nonspherical asteroid. J. Guid. Control Dyn. **36**(3), 790–798 (2013)

Hudson, R.S., Ostro, S.J.: Shape of asteroid 4769 castalia, (1989 PB) from inversion of radar images. Science **263**(1994), 940–943 (1989)

Jones, B.A., Born, G.H., Beylkin, G.: A Cubed Sphere Gravity Model for Fast Orbit Propagation, pp. 09–137. American Astronomical Society, Washington, DC (2009)

Jones, B.A., Efficient Models for the Evaluation and Estimation of the Gravity Field, Ph.D. thesis, The University of Colorado at Boulder (2010)

Kaula, W.M.: Theory of Satellite Geodesy, chap. 1. Blaisdell Publishing Company, Waltham, Massachusetts (1966)

Kholchevnikov, C.: Le développement du potentiel dans le cas d'une densité analytique. Celest. Mech. **3**, 232–240 (1971)

Kholchevnikov, C.: Le développement du potentiel dans le cas d'une densité lisse. Celest. Mech. **6**, 214–220 (1972)

Kholshevnikov, C.: On convergence of an asymmetrical body potential expansion in spherical harmonics. Celest. Mech. **16**, 45–60 (1977)

Liu, H., Zou, J.: Zeros of the Bessel and spherical Bessel functions and their applications for uniqueness in inverse acoustic obstacle scattering. J. Appl. Math. **72**, 817–831 (2007)

Lundberg, J.B., Schutz, B.E.: Recursion formulas of Legendre functions for use with nonsingular geopotential models. J. Guid. Control Dyn. **11**, 31–38 (Feb. 1988)

MacRobert, T.M.: Spherical Harmonics: An Elementary Treatise on Harmonic Functions with Applications, chap. 2, 4, 6, 8, 14, 2nd edn. Dover Publications Inc, NY (1948)

Nolan, M., Magri, C., Howell, E., Benner, L.A.M., Giorgini, J.D., Hergenrother, C., Hudson, R., Lauretta, D., Margot, J.-L., Ostro, S., Scheeres, D.: Shape model and surface properties of the OSIRIS-REx target asteroid (101955) Bennu from radar and lightcurve observations. Icarus **226**, 629–640 (2013)

Ostro, S.J., Chandler, J.F., Hine, A.A., Rosema, K.D., Shapiro, I.I., Yeomans, D.K.: Radar images of asteroid 1989 PB. Science **248**, 1523–1528 (1990)

Palmer, P.L.: Stability of Collisionless Stellar Systems—mechanisms For The Dynamical Structure of Galaxies, chap. 10, pp. 181–190. Kluwer Academic Publishers, Dordrecht (1994)

Park, R.S., Werner, R.A., Bhaskaran, S.: Estimating small-body gravity field from shape model and navigation data. J. Guid. Control Dyn. **33**, 212–221 (2010)

Pinsky, M.A.: Introduction to Partial Differential Equations with Applications, chap. 0, 2, 3, 4. MacGraw-Hill Book Company, NY (1984)

Russell, R.P., Arora, N.: Global Point Mascon Models for Simple. Accurate and Parallel Geopotential Computation, pp. 11–158. AAS/AIAA Space Flight Mechanics Meeting (2011)

Takahashi, Y., Scheeres, D.: Generalized density distribution estimation for small bodies. In: 23rd AAS/AIAA Space Flight Mechanics Meeting, No. 13–265 (2013)

Takahashi, Y., Scheeres, D.: Surface Gravity Fields for Asteroids and Comets. In: 22nd AAS/AIAA Space Flight Mechanics Meeting (2012)

Takahashi, Y., Scheeres, D., Werner, R.A.: Surface gravity fields for asteroids and comets. J. Guid. Control Dyn. **36**(2), 362–374 (2013)

Tapley, B.D., Schutz, B.E., Born, G.H.: Statistical Orbit Determination. Elsevier Academic Press, Amsterdam (2004)

Watson, C.: A Treatise on the Theory of Bessel Functions, chap. 2, 3, 15, 2nd edn. Cambridge University Press, Cambridge (1944)

Werner, R.A.: Evaluating Descent and Ascent Trajectories Near Non-Spherical Bodies. Tech. Rep. http://www.techbriefs.com/component/content/article/8726, Jet Propulsion Laboratory (2010)

Werner, R.A., Scheeres, D.J.: Exterior gravitation of a polyhedron derived and compared with harmonic and mascon gravitation representations of asteroid 4769 castalia. Celest. Mech. Dyn. Astron. **65**, 314–344 (1997)

Werner, R.A.: Spherical Harmonic coefficients for the potential of a constant-density polyhedron. Comput. Geosci. **23**(10), 1071–1077 (1997)